



OPEN Stability analysis of grid-connected hydropower plant considering turbine nonlinearity and parameter-varying penstock model

Chen Feng^{1,2,6}, Na sun^{1,6}, Chuang Zheng¹, Yongqi Zhu¹, Nan Zhang^{1,3}✉, Yahui Shan⁴✉, Liping Shi¹ & Xiaoming Xue⁵

This paper aims to investigate the nonlinear stability and dynamic characteristics of the grid-connected hydro-turbine governing system (GCHTGS) considering the parameter-varying model (PVM) of penstock and turbine nonlinearity. Considering the inertia of fluid flow and water head loss of the penstock, a novel PVM of penstock with higher precision and simpler form is proposed, where the parameter determination process is developed to simplify the transcendental function of PVM. The accuracy of PVM has been sufficiently validated by numerical simulation. BP neural networks (BPNN) are used to establish the nonlinear model of the hydro-turbine. The NN-based differentiation method (NND) is adopted to obtain the transfer coefficients of the linear hydro-turbine model under full operating conditions (FOC). The nonlinear state space equations of GCHTGS with PVM and variable transfer coefficients are established. First, the influence of different penstock models on stability is investigated, and the comparison results show that the proposed PVM has a more precise stability region. Then the influence laws of operation conditions on the stability of GCHTGS are revealed. Finally, based on sensitivity analysis, qualitative and quantitative analyses of the effect of parameters on stability and dynamic characteristics are performed. This work establishes a more precise nonlinear GCHTGS model and provides a better understanding of the influence of hydro-turbine nonlinearity on the stability and parameter sensitivity of GCHTGS.

Keywords Grid-connected hydro-turbine governing system, Parameter-varying penstock model, Nonlinear hydro-turbine, Stability analysis, Sensitivity analysis, Full operating conditions

Abbreviations

| | |
|--------|---|
| GCHTGS | Grid-connected hydro-turbine governing system |
| PVM | Parameter-varying model |
| BPNN | BP neural networks |
| NND | NN-based differentiation method |
| FOC | Full operation conditions |
| RE | Renewable energy |
| PG | Power grid |
| HTGS | Hydro-turbine governing system |
| GVO | Guide vane opening |
| RWHM | Rigid water hammer model |
| EWHM | Elastic water hammer model |
| TM | Transcendental model |
| DRP | Dynamic response process |
| HBT | Hopf bifurcation theory |
| GWO | Grey wolf optimizer algorithm |

¹Jiangsu Key Laboratory of Advanced Manufacturing Technology, Huaiyin Institute of Technology, Huai'an 223003, China. ²College of Energy and Electrical Engineering, Hohai University, Nanjing 211100, China. ³Beijing Huairou Laboratory, Beijing 101400, China. ⁴Wuhan Second Ship Design and Research Institute, Wuhan 430064, China. ⁵School of Intelligent Manufacturing Jiangsu College of Engineering and Technology, Nantong 226006, China. ⁶Chen Feng and Na sun contributed equally to this work. ✉email: zhangnanhust@163.com; shanyahui@hust.edu.cn

List of symbols

| | |
|------------------------|---|
| T_w | Flow inertia time constant of penstock, s |
| T^e | Water elasticity coefficient |
| f | Relative deviation of head loss of penstock |
| K_p | Proportional gain |
| K_I | Integral gain |
| K_D | Differential gain |
| M_t | Kinetic moment, N · m |
| Q_t | Discharge in pump-turbine, m ³ /s |
| y | Relative deviation of guide vane opening |
| x_t | Relative deviation of turbine unit speed |
| h | Relative deviation of pump-turbine head |
| m_t | Relative deviation of kinetic moment |
| q_t | Relative deviation of discharge in pump-turbine |
| $e_x e_y e_h$ | Moment transfer coefficients of turbine |
| $e_{qy} e_{qx} e_{qh}$ | Discharge transfer coefficients of turbine |
| T_a | Turbine unit inertia time constant, s |
| T_y | Time constant of the primary servo-system, s |
| b | Permanent speed droop |
| m_p | Relative deviation of resisting moment |
| e_g | Load self-regulation coefficient |
| K_a | Equivalent synchronization coefficient |
| $\xi_1 \xi_2$ | Intermediate state variables |
| D_a | Equivalent damping coefficient load self-regulation coefficient |
| x_s | Relative deviation of grid frequency |
| T_s | Equivalent permanent difference coefficient of power grid |
| B | Power conversion factor |
| D_s | Self-regulating coefficient of equivalent load of power grid |
| T_g | Inertia time constant of power grid equivalent unit, s |
| R_g | Equivalent permanent difference coefficient of power grid |
| w | Angular frequency |
| σ | Varying parameter |
| w_T | First peak of the frequency response |

The importance of the stability of hydropower station

A new round of global energy and technological revolution has evolved in depth, and the vigorous development of renewable energy (RE) has become a major strategic direction for the global energy transition and climate change¹. To combat climate change and curb global warming, China has proposed the goals of “carbon peak” and “carbon neutrality”². However, RE sources such as wind and solar have strong randomness, volatility, and uncertainty, and their large-scale grid connection will seriously threaten the safe and stable operation of the power grid (PG)³. In the PG, hydropower plays a crucial role in the PG’s power balancing and regulation, effectively reducing the effect of intermittent RE^{4–6}. Therefore, the most fundamental and essential task is to guarantee that hydropower systems continue to function in a stable manner.

Related work

The hydro-turbine governing system (HTGS) is a complex system consisting of hydraulic, mechanical, and electrical components. It functions as the primary control system for hydropower stations⁷. Each component of HTGS affects the stability and dynamic performance of HTGS. The hydro-turbine is the core equipment of a hydropower station. It converts the kinetic energy of water flow into mechanical energy, which is then transformed into electrical energy through the generator⁸. The hydro-turbine significantly affects the hydropower station’s energy conversion efficiency and operational stability. The hydro-turbine is a highly nonlinear, time-varying, and non-minimum phase system, with parameters that vary with operating conditions. Due to the strong nonlinearity of hydro-turbine, the turbine’s torque and discharge are described as nonlinear functions of water head, unit speed and guide vane opening (GVO), which significantly complicate the stability and dynamic characteristics of HTGS⁹. However, for small perturbations around a stable equilibrium operating point, the hydro-turbine can be approximated as linear, and a linearized model can be derived¹⁰. The linear model of the hydro-turbine with fixed transfer coefficients is widely used due to its simplicity^{11–16}.

The design of long or super long water diversion penstock has obvious advantages in terms of efficient use of water resources, improved power generation efficiency, and economic benefits, and it has become a standard practice in the design of modern hydropower stations¹⁷. The penstock system is the core component of HTGS, and its accurate modeling is essential for stability analyses. For a long penstock, the transcendental function can be used to describe its dynamic characteristics accurately. Nevertheless, the transcendental function is impractical for theoretical analyses due to its complexity¹⁸. Therefore, the Taylor series is used to expand the transcendental model (TM), and lower-order approximation models are commonly employed for stability analyses. The approximation models can be classified into the rigid water hammer model (RWHM) and the elastic water hammer model (EWHM)^{19,20}. The RWHM neglects the water elasticity and is suitable for short penstock. For a long penstock, the EWHM usually is used. However, although low-order approximation models are commonly used in theoretical analyses, their accuracy is not guaranteed²¹.

The stability of HTGS is strongly influenced by hydro-turbine nonlinearity and water elasticity. However, current studies primarily focus on the HTGS's stability using RWHM and linear hydro-turbine. Guo et al.²² study the stability of water power-speed control system for hydropower station with air cushion surge chamber. The findings indicate that the hydro-turbine negatively affects the system. Nonetheless, Ref.²² adopts the linear hydro-turbine model. Guo et al.^{12,23–28} systematically studied the stability of the HTGS with different ceiling tailrace tunnel and surge chamber. However, these studies are limited to the linear hydro-turbine model and RWHM. Xu et al.²⁹ study the stability of HTGS considering nonlinear turbine characteristics. The effect of turbine linearity on the stability and dynamic response of HTRS is investigated. However, the research is limited to a narrow range of full operating conditions (FOC), and the effect of operating conditions variations (GVO and water head) on the stability of HTGS has not been studied. And the elastic water hammer is not considered. Ling et al.³⁰ conducted the Hopf bifurcation analysis of HTGS with elastic water hammer effect. The study indicates that the water hammer elasticity has an unfavorable effect on the system stability, especially for the long penstock. However, the reliability of such a model cannot be ensured.³¹ In Ref.³², a parameter-varying penstock model with higher precision and simpler form is proposed for the theoretical analyses. However, the head loss is ignored and a linear hydro-turbine model is considered.

Parameter sensitivity analysis comprises local sensitivity analysis and global sensitivity analysis, local sensitivity analysis can only reflect the impact of a single parameter change on the system output, while global sensitivity analysis can effectively reflect the impact of simultaneous changes in multiple parameters on the system output. For an asymmetric HTGS, Lai et al.³³ reveal the effect of system parameters and water diversion layout on the stability of HTGS based on local sensitivity analysis method. Guo et al.³⁴ employ local sensitivity analysis method to study the parameter sensitivity of variable-speed pumped storage power station.

In summary, a great deal of important work has been done to ensure the stability of HTGS. But there's still a lot of space for advancement and improvement. Here are some of the research gaps:

- (1) For stability analysis, the majority of the existing literature use a linearized hydro-turbine model on a specific operating condition under small disturbances. However, a hydro-turbine's parameters and operating characteristics vary with operating conditions. Most previous studies are limited to a specific operating condition of HTGS without considering other operating conditions. The influence of operating conditions on HTGS stability remains unexplored. Therefore, it is essential to develop a nonlinear hydro-turbine model under FOC.
- (2) In the present study, the RWHM of the penstock system is widely applied in the stability and dynamic characteristics analysis of HTGS. The effects of water elasticity and head loss, which have a significant impact on the stability of HTGS, are neglected in most papers. Although the universal EWHM considers the elasticity of water flow, its modeling accuracy can't be guaranteed. Hence, the traditional HTGS model used for dynamic and stability analysis has limitations. Developing a more accurate HTGS model with a precise penstock model is essential for stability analysis.
- (3) Although many research papers have adequately discussed the sensitivity of hydraulic, mechanical, and electrical parameters on the stability of HTGS, these studies only focus on the variation of a single parameter based on the local sensitivity analysis method, ignoring the interaction between parameters. Moreover, parameter sensitivity is often analyzed qualitatively, without precise quantitative metrics.

This paper aims to establish a refined model of grid-connected HTGS (GCHTGS) considering hydro-turbine nonlinearity and an accuracy penstock model and to study the stability of the system under FOC. Further, both local and global sensitivity analysis methods are used to study the parameter sensitivity of GCHTGS. The following are the contributions and novelty of this paper:

- (1) Considering the hydro-turbine nonlinearity, the BPNN³⁵ is used to describe the complex nonlinearity of a hydro-turbine. Then the NND is adopted to obtain the piecewise linearized model under FOC. Hence, the impact of operational conditions on the stability and dynamic characteristics of GCHTGS can be elucidated.
- (2) This paper proposes a more precise and simpler PVM for stability analyses that takes head loss and water elasticity into account. The experimental results show that the proposed penstock model has higher precision based on numerical simulation and stability analysis. Therefore, a refined model of GCHTGS can be established based on the piecewise linearized hydro-turbine model and the proposed penstock model. More accurate stability and dynamic characteristics can be obtained.
- (3) Both local and global sensitivity analysis methods are adopted simultaneously to conduct the parameter sensitivity analysis of GCHTGS. The sensitivity of a single parameter and the coupling effect between parameters are accurately quantified and analyzed, which can be applied to direct the GCHTGS's construction and functionality.

Research aims

The research mainly focuses on the following key questions:

- (1) How to consider the nonlinearity of the hydro-turbine and study the stability of GCHTGS under FOC?
- (2) Which penstock model is best suited for examining the stability of GCHTGS from the perspective of model accuracy and complexity?
- (3) How to quantify the sensitivity of a single parameter and the coupling effect between parameters on the GCHTGS, and guide the high-quality operation of the system.

This paper is organized as follows: The mathematical model of the GCHTGS system considering hydro-turbine nonlinearity and a parameter-varying penstock model, is established in Section "Mathematical of GCHTGS". The stability analysis method based on the Hopf bifurcation theory (HBT) is introduced in Section "Stability analysis of GCHTGS", the stability region of the system is determined and verified by numerical simulation. In addition, the influence mechanisms of different penstock models and operation conditions (GVO and water head) on the stability of the system are revealed. In Section "Sensitivity analysis", sensitivity analysis of GCHTGS is conducted. In Section "Conclusions and future research directions" conclusions are given.

Mathematical of GCHTGS

In this study, the GCHTGS mainly consists of an upstream reservoir, penstock, governor, hydro-turbine, generator, downstream reservoir and PG, as shown in Fig. 1. The basic mathematical equations of all subsystems of the GCHTGS coupling system are presented below.

Previous penstock models

Penstock is one of the important components of GCHTGS. The opening or closing of the guide vanes in the pressure penstock will result in an abrupt change in flow. Due to the inertia and compressibility of the water body, the water head in the penstock will change violently and periodically.

Taking into account the water elasticity and head loss, the transcendental function of the long penstock is as follows

$$G_{P0}(s) = -\frac{T_w}{T_e} \tanh(T_e s + f) \quad (1)$$

From Eq. (1), it can be seen that the mathematical model of the penstock system is a hyperbolic tangent function, which is not suitable for theoretical stability analysis. Therefore, Eq. (1) is expanded using the Taylor series:

$$\tanh(x) = \frac{sh(x)}{ch(x)} = \frac{x + \frac{1}{3!}x^3 + \dots}{1 + \frac{1}{2!}x^2 + \frac{1}{4!}x^4 + \dots} \quad (2)$$

Different order transfer function models can be obtained. The first-order RWHM is widely used when the length of penstock is short:

$$G_{P1}(s) = -T_w s - \frac{T_w}{T_e} f \quad (3)$$

When the GCHTGS has a long penstock, a more accurate model is needed to describe the water hammer process. Therefore, the second-order EWHM and fourth-order EWHM are considered as:

$$G_{P2}(s) = -\frac{T_w}{T_e} \frac{f + T_e s}{1 + f T_e s + \frac{1}{2} T_e^2 s^2} \quad (4)$$

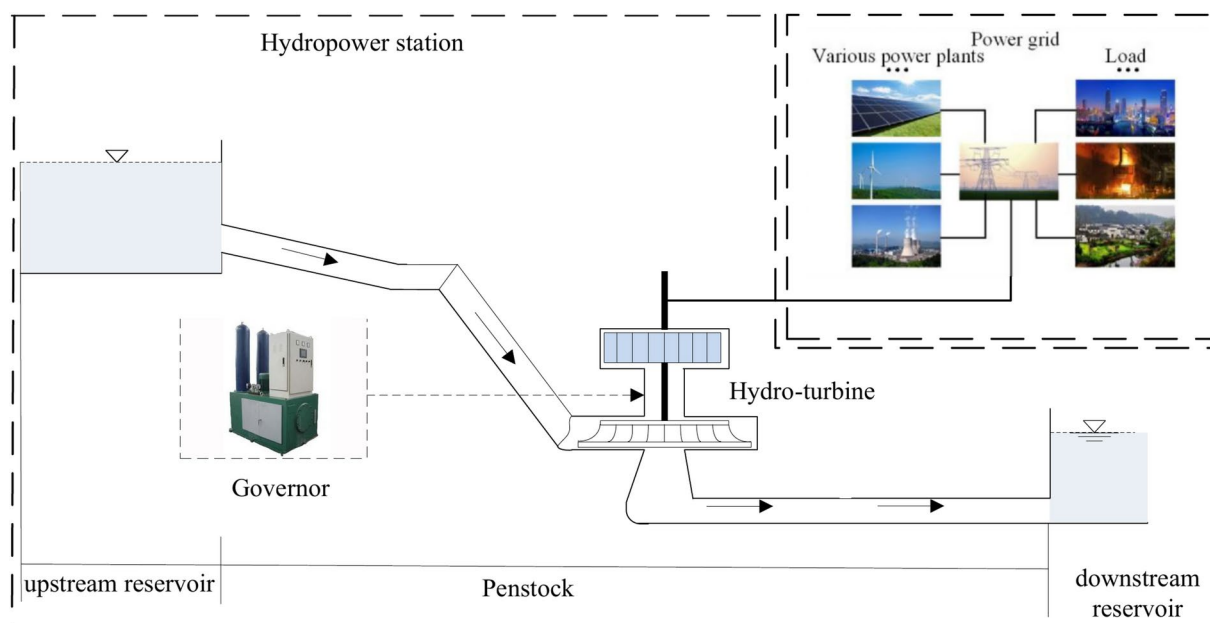


Fig. 1. Schematic diagram of GCHTGS.

$$G_{P3}(s) = -\frac{T_w}{T_e} \frac{f + T_e s + \frac{1}{2} f T_e^2 s^2 + \frac{1}{6} T_e^3 s^3}{1 + f T_e s + \frac{1}{2} T_e^2 s^2 + \frac{1}{6} f T_e^3 s^3 + \frac{1}{24} T_e^4 s^4} \quad (5)$$

Parameter-varying penstock model

It can be observed that the model accuracy improves with the increase in order, but too high an order will not only increase the calculation complexity, but also cause oscillation distortion in the time-domain response³⁶. Liu et al.³⁶ proposed a reduced-order EWHM shown in Eq. (1).

$$\begin{cases} G_{P4}(s) = -\frac{T_w}{T_e} \frac{(\frac{2fT_e^2}{\pi^2} s^2 + T_e s + f) w_n^2}{s^2 + 2\xi w_n s + w_n^2} \\ \xi = \frac{e^f - e^{-f}}{2(e^f + e^{-f})} \sqrt{f^2 + \frac{\pi^2}{4}} \\ w_n = \frac{\pi}{2T_e} \end{cases} \quad (6)$$

Compared with the second-order EWHM, it correctly expresses the frequency domain resonance peak and increases the effective approximation region from 1 rad/s to 2 rad/s. At the same time, it avoids the problem of time-domain oscillation distortion caused by fourth-order EWHM, thus more reasonably describing the water hammer process in pressure pipe. By comparing the frequency-domain characteristics of Eq. (1) and Eq. (6), it can be found that the reduced-order EWHM has a higher accuracy when the water elasticity coefficient T_e is small. However, a large error is unavoidable when the T_e is large, as shown in Fig. 2. The error between Eq. (1) and Eq. (6) increases with the increase of T_e .

Therefore, we propose a PVM as follows:

$$G_{P5}(s) = -\frac{T_w}{T_e} \frac{(\frac{2fT_e^2}{\pi^2} s^2 + T_e s + f) w_n^2}{\sigma s^2 + 2\xi w_n s + w_n^2} \quad (7)$$

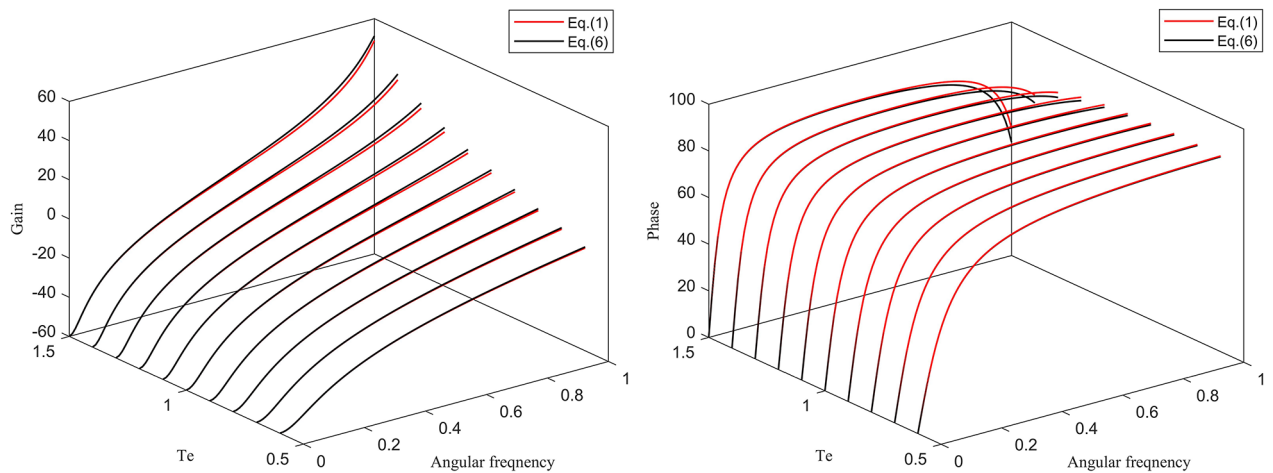
In Ref.³⁶, the parameter σ was set as a constant, which is determined by equating the frequency of the poles of the simplified and original models w_T ($w_T = \pi/2T_e$). Therefore, the model Eq. (6) has higher accuracy at w_T , but the maximum response frequency w_s is usually less than w_T when the frequency regulations of GCHTGS are under normal operating conditions³². Therefore, the parameter σ determination method needs to be proposed.

The amplitude and frequency characteristics of the transfer functions Eq. (1) and Eq. (7) can be obtained by inserting $s = jw$:

$$G_{P0}(jw) = -\frac{T_w}{T_e} \frac{1 - e^{-2f} e^{-j2T_e w}}{1 + e^{-2f} e^{-j2T_e w}} = -\frac{T_w}{T_e} \frac{1 - e^{-2f} \cos(2T_e w) + j e^{-2f} \sin(2T_e w)}{1 + e^{-2f} \cos(2T_e w) - j e^{-2f} \sin(2T_e w)} \quad (8)$$

$$G_{P5}(jw) = -\frac{T_w}{T_e} \frac{(-\frac{2fT_e^2}{\pi^2} w^2 + j T_e w + f) w_n^2}{-\sigma w^2 + j 2\xi w_n w + w_n^2} \quad (9)$$

To obtain a suitable σ , an error function between Eq. (8) and Eq. (9) is defined as follows:



(a) Amplitude frequency characteristics

(b) Phase frequency characteristics

Fig. 2. Frequency-domain characteristics with different values of T_e .

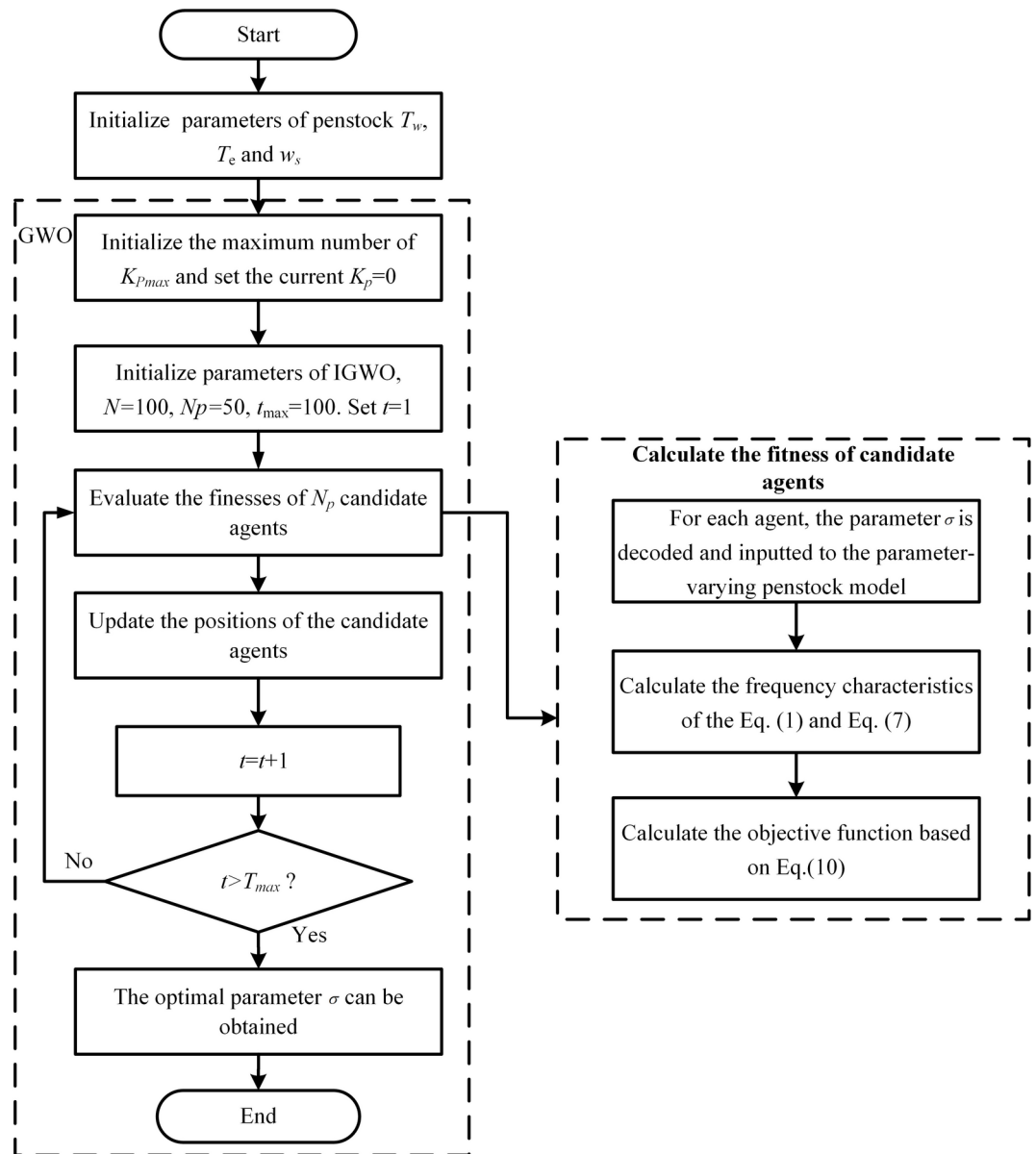


Fig. 3. Flow chart of the the calculation steps of σ .

| w_s/w_T | 0.1 | 0.2 | 0.3 | 0.4 | 0.5 | 0.6 | 0.7 | 0.8 | 0.9 |
|-----------|--------|--------|--------|--------|--------|--------|--------|--------|--------|
| σ | 0.7551 | 0.8122 | 0.8257 | 0.8359 | 0.8471 | 0.8609 | 0.8785 | 0.9013 | 0.9328 |

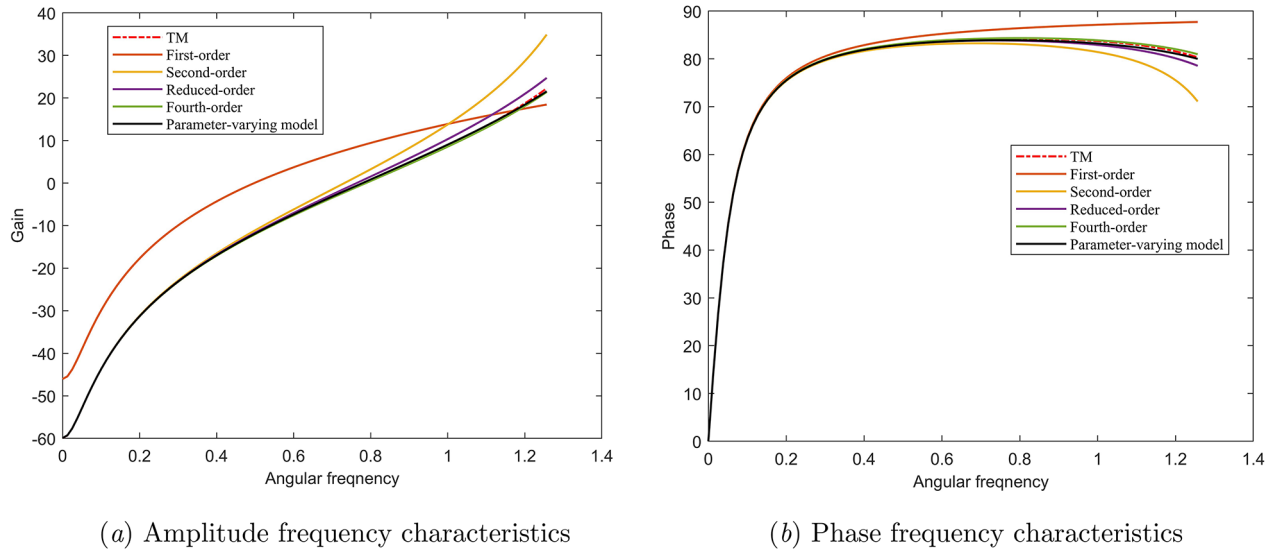
Table 1. Varying parameters of the model.

$$E = \sum_{k=1}^N (|G_{P0}(jw_k)| - |G_{P5}(jw_k)|)^2 \quad (10)$$

where w_k is an angular frequency range $[0, w_s]$. The σ can be obtained by minimizing the objective function based on the Grey Wolf Optimizer (GWO) algorithm³⁷, the calculation steps are shown in Fig. 3.

Choosing $T_w = 2$, $T_e = 1$ and $f = 0.05$, under different values of w_s , the values of the parameter σ are calculated and shown in Table 1. The errors between Eq. (6) and Eq. (1), Eq. (7) and Eq. (1) are shown in Table 2. From Table 1, we can find that the parameter σ varies with w_s , so Eq. (7) is called a parameter-varying model (PVM), where different hydropower stations have different values of σ . From Table 1, with the increases of w_s , the error

| Eq\ w_s/w_T | 0.1 | 0.2 | 0.3 | 0.4 | 0.5 | 0.6 | 0.7 | 0.8 | 0.9 |
|---------------|--------|--------|--------|--------|---------|---------|---------|----------|----------|
| Equation (6) | 0.0576 | 0.489 | 2.2642 | 7.0311 | 17.2382 | 36.2739 | 68.5904 | 119.4283 | 190.2848 |
| Equation (7) | 0.0083 | 0.0061 | 0.0066 | 0.0144 | 0.0561 | 0.2477 | 1.0545 | 4.4142 | 20.095 |

Table 2. Overall errors of Eq. (6) and Eq. (7) compared with Eq. (1).**Fig. 4.** Frequency-domain characteristics under different penstock models.

increases. Compared with the reduced-order EWHM, the proposed PVM has smaller errors under different w_s . Therefore, the proposed PVM has higher accuracy.

Choosing $w_s/w_T=0.8$, the frequency-domain characteristics of the TM defined by Eq. (1), the first-order RWHM, the second-order EWHM, the reduced-order EWHM, the fourth-order EWHM and the PVM is shown in Fig. 4. From Fig. 4, it is clearly demonstrated that the frequency characteristic curves of TM, fourth-order EWHM and the proposed PVM are almost coincident. The results indicate that the fourth-order EWHM and PVM have coincident model accuracy. The model accuracy of first-order RWHM, second-order EWHM, reduced-order EWHM and fourth-order EWHM increases gradually. Compared with fourth-order EWHM, the PVM has a lower model order while ensuring sufficient accuracy. Consequently, the proposed PVM outperforms the conventional penstock model.

Governor

The classical PI controller is adopted for GCHTGS in this paper, which is defined as follows:

$$G_{PI}(s) = K_P + \frac{K_I}{s} \quad (11)$$

Hydro-turbine

NN model of hydro-turbine

An accurate analytical mathematical model of the hydro-turbine has not yet been obtained due to its complex characteristics. Its dynamic characteristics are typically expressed as³⁸:

$$\begin{cases} M_t = M_t(y, x_t, H) \\ Q_t = Q_t(y, x_t, H) \end{cases} \quad (12)$$

The nonlinear hydro-turbine model given in Eq. (12) can be linearized using Taylor series expansion for small disturbances near a steady-state operating point. Equation (12) can be rewritten as³⁹:

$$\begin{cases} m_t = e_y y + e_x x_t + e_h h \\ q_t = e_{qy} y + e_{qx} x_t + e_{qh} h \end{cases} \quad (13)$$

where $e_h = \partial m_t / \partial h$, $e_x = \partial m_t / \partial x_t$, $e_y = \partial m_t / \partial y$, $e_{qh} = \partial q_t / \partial h$, $e_{qx} = \partial q_t / \partial x_t$, $e_{qy} = \partial q_t / \partial y$ the transfer coefficients of torque and discharge, respectively;

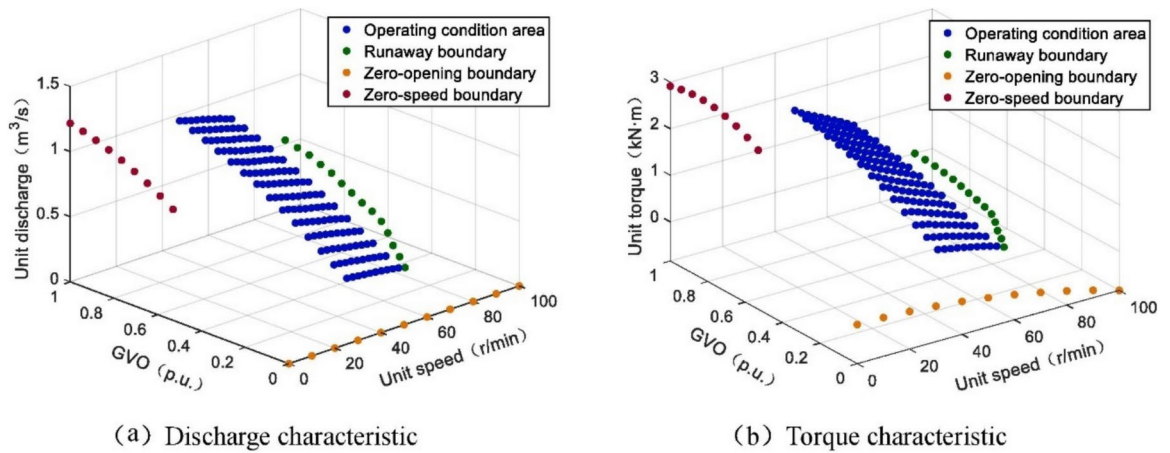


Fig. 5. Test data of hydro-turbine.

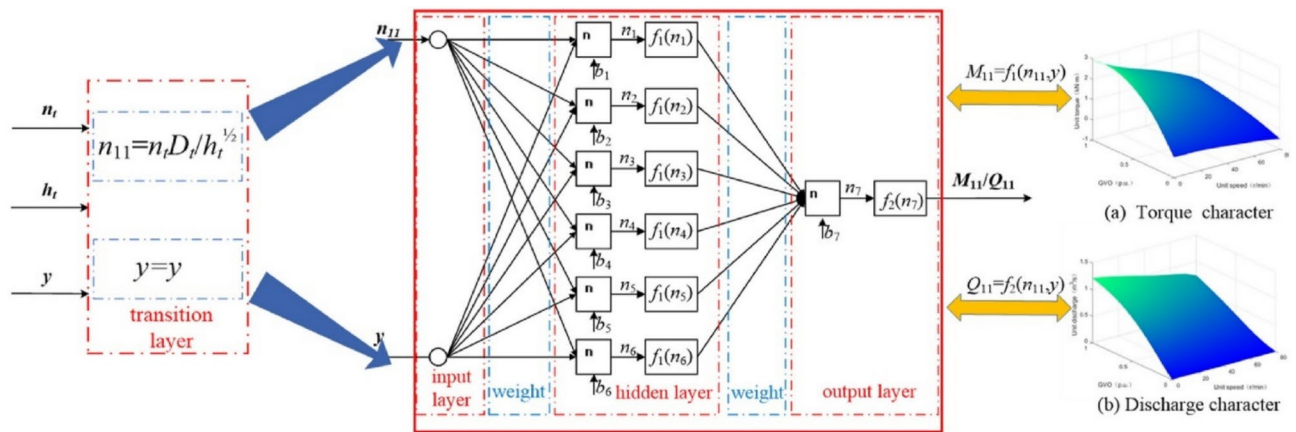


Fig. 6. The training process of BPNN.

The six-coefficient model of the hydro-turbine represents a linearized model under specific operating conditions (determined by water head and GVO). Experimental results based on the linear model are inaccurate and cannot be generalized to other operating conditions. Therefore, the six coefficients under different operating conditions must be determined to analyze stability under FOC. A specific actual measured data of the hydro-turbine is shown in Fig. 5. However, the measured data of the hydro-turbine is incomplete, particularly for small openings and low head conditions.

NN possess powerful nonlinear modeling capability and adaptability. They can learn and capture complex patterns and correlations in data, demonstrating excellent generalization ability for prediction tasks involving unknown scenarios and new samples. Consequently, they have been widely used in various fields. In this paper, considering the strong nonlinearity and the missing data of the hydro-turbine, the BPNN is used to fit the torque and discharge data. The BPNN training process and hydro-turbine BPNN models are illustrated in Fig. 6 and Fig. 7, respectively. Figure 7 shows that the GVO lines are effectively extended and refined.

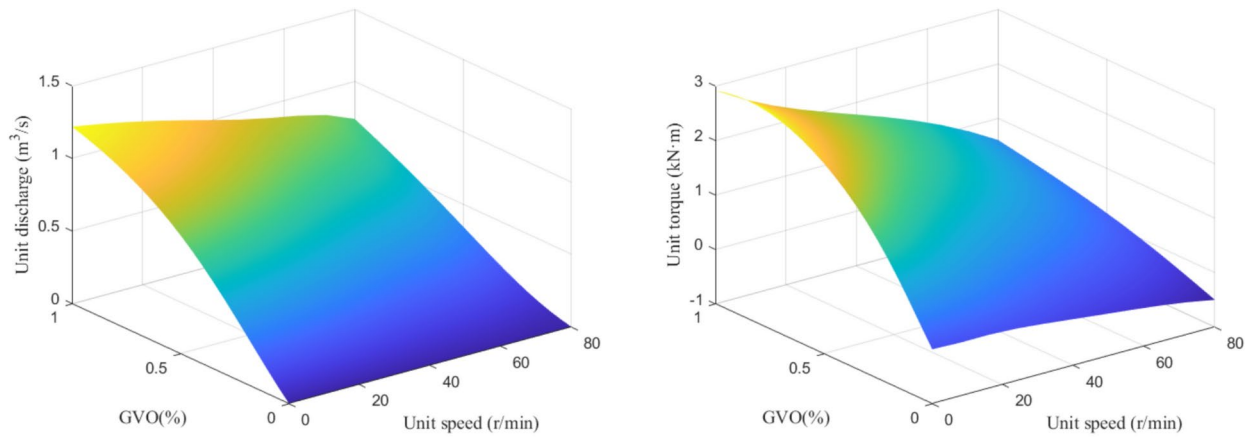
Transfer coefficients calculation of hydro-turbine

A novel approach based on the NND is proposed by Liu et al.⁴⁰ to determine the six transfer coefficients of hydro-turbines. The steps of the method are as follows.

- (1) Discharge and torque can be obtained based on the BPNN models:

$$\begin{cases} Q = f_Q(n_{11}, Y) D^2 \sqrt{H} \\ M_t = f_M(n_{11}, Y) D^3 H \end{cases} \quad (14)$$

- (2) The Eq. (14) can be rewritten as follows:



(a) Discharge characteristic

(b) Torque characteristic

Fig. 7. BPNN models of Hydro-turbine.

$$\begin{cases} Q = f_{q2}(w_{q2} \cdot f_{q1}(w_{q1}I + b_{q1}) + b_{q2}) D^2 \sqrt{H} n \\ M_t = f_{m2}(w_{m2} \cdot f_{m1}(w_{m1}I + b_{m1}) + b_{m2}) D^3 H n \end{cases} \quad (15)$$

where, $w_{q1}(w_{m1})$ and $w_{q2}(w_{m2})$ represent the weights of the hidden layer and the output layer of the neural network, respectively. $f_{q1}(f_{m1})$ and $f_{q2}(f_{m2})$ denote the activation functions used in the hidden layer and the output layer of the neural network, respectively. $b_{q1}(b_{m1})$ and $b_{q2}(b_{m2})$ represent the thresholds of the hidden layer and the output layer of the neural network, respectively; $I = (n_{11}, Y)$ is the input of the neural network.

(3) Taking the partial derivatives of the previous functional relationship, we obtain the general expression for the transfer coefficients.

$$\begin{cases} e_{qy} = \frac{Y_m}{Q_r} \frac{\partial Q}{\partial Y} = \frac{Y_m}{Q_r} D^2 \sqrt{H} f'_{q2} w_{q2} f'_{q1} w_{q1} \frac{\partial I}{\partial Y} \\ e_{qh} = \frac{H_r}{Q_r} \frac{\partial Q}{\partial H} = \frac{H_r}{Q_r} \left(\frac{D^2}{2\sqrt{H}} f_Q + D^2 \sqrt{H} f'_{q2} w_{q2} f'_{q1} w_{q1} \frac{\partial I}{\partial H} \right) \\ e_{qx} = \frac{X_r}{Q_r} \frac{\partial Q}{\partial X} = \frac{X_r}{Q_r} D^2 \sqrt{H} f'_{q2} w_{q2} f'_{q1} w_{q1} \frac{\partial I}{\partial X} \\ e_y = \frac{Y_m}{M_r} \frac{\partial M_t}{\partial Y} = \frac{Y_m}{M_r} D^3 H f'_{m2} w_{m2} f'_{m1} w_{m1} \frac{\partial I}{\partial Y} \\ e_h = \frac{H_r}{M_r} \frac{\partial M_t}{\partial H} = \frac{H_r}{M_r} \left(D^3 f_M + D^3 H f'_{m2} w_{m2} f'_{m1} w_{m1} \frac{\partial I}{\partial H} \right) \\ e_x = \frac{X_r}{M_r} \frac{\partial M_t}{\partial X} = \frac{X_r}{M_r} D^3 H f'_{m2} w_{m2} f'_{m1} w_{m1} \frac{\partial I}{\partial X} \end{cases} \quad (16)$$

Generator and Load

For the GCHTGS, the second-order synchronous generator model is adopted, and its differential equations are shown⁴¹:

$$\begin{cases} T_a \frac{dx_t}{dt} = m_t - (e_g x_t + K_a \xi_1 + D_a (x_t - x_s) + m_g) \\ \frac{d\xi_1}{dt} = x_t - x_s \end{cases} \quad (17)$$

Power grid

To analyze the stability of the GCHTGS system, it is necessary to establish a simple PG mathematical model that can reflect the load and frequency characteristics. In this paper, the PG is modeled an equivalent generator and its linear model can be obtained. The detailed structure of the simplified PG is shown in Fig. 8. If the load disturbance of the PG is ignored, i.e., $\Delta p_g = 0$, the basic equation of the power grid is:

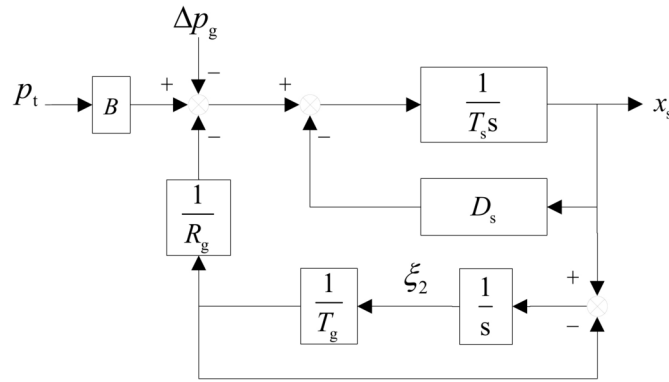


Fig. 8. Block diagram of the equivalent PG.

$$\begin{cases} \frac{dx_s}{dt} = \frac{1}{T_s} \left(Bp_t - D_s x_s - \frac{1}{T_g R_g} \xi_2 \right) \\ \frac{d\xi_2}{dt} = x_s - \frac{1}{T_g} \xi_2 \end{cases} \quad (18)$$

By combining Eq. (7), Eq. (11), Eq. (13), and Eq. (17)–(18), the state equation of GCHTGS considering the proposed PVM can be obtained as Eq. (19). It should be noted that r_1 and r_2 are the intermediate state variables. Similarly, the state equations of GCHTGS with first-order RWHM, second-order EWHM and fourth-order EWHM are reported as Eq. (20)–(22).

$$\begin{cases} \dot{x}_t = \frac{1}{T_a} [e_y y + (e_x - e_g - D_a)x_t + e_h h - K_a \xi_1 + D_a x_s - m_g] \\ \dot{y} = - \left[\frac{K_P}{T_a} (e_x - e_g - D_a) + K_I \right] x_t - \frac{K_P}{T_a} [e_y y + e_h h - K_a \xi_1 + D_a x_s - m_g] \\ \dot{x}_s = \frac{1}{T_s} \left[D_a B x_t - (D_s + D_a B) x_s + K_a B \xi_1 - \frac{1}{R_g T_g} \xi_2 \right] \\ \dot{\xi}_1 = x_t - x_s \\ \dot{\xi}_2 = x_s - \frac{1}{T_g} \xi_2 \\ \dot{r}_1 = r_2 \\ \dot{r}_2 = \frac{-2\xi w_n}{\alpha} r_2 - \frac{w_n^2}{\alpha} r_1 + e_{qx} x_t + e_{qy} y + e_{qh} h \\ \dot{h} = - \frac{T_w f w_n^2}{T_e \alpha} r_1 - \frac{T_w w_n^2}{\alpha} r_2 \end{cases} \quad (19)$$

$$\begin{cases} \dot{x}_t = \frac{1}{T_a} [e_y y + (e_x - e_g - D_a)x_t + e_h h - K_a \xi_1 + D_a x_s - m_g] \\ \dot{y} = - \left[\frac{K_P}{T_a} (e_x - e_g - D_a) + K_I \right] x_t - \frac{K_P}{T_a} [e_y y + e_h h - K_a \xi_1 + D_a x_s - m_g] \\ \dot{x}_s = \frac{1}{T_s} \left[D_a B x_t - (D_s + D_a B) x_s + K_a B \xi_1 - \frac{1}{R_g T_g} \xi_2 \right] \\ \dot{\xi}_1 = x_t - x_s \\ \dot{\xi}_2 = x_s - \frac{1}{T_g} \xi_2 \\ \dot{h} = x_t \left(\frac{e_{qx} - e_{qy} K_P}{T_a e_{qh}} D_a + \frac{e_{qy} K_P - e_{qx}}{T_a e_{qh}} (e_x - e_g) + \frac{K_i e_{qy}}{e_{qh}} + \frac{f e_{qx} T_w}{e_{qh} T_e} \right) \\ + x_s \left(\frac{e_{qy} K_P - e_{qx}}{T_a e_{qh}} D_a \right) + \xi_1 \left(\frac{K_a e_{qx}}{T_a e_{qh}} - \frac{K_a e_{qy} K_P}{T_a e_{qh}} \right) + \frac{e_{qx} - e_{qy} K_P}{T_a e_{qh}} m_g \\ + h \left(\frac{e_{qy} K_P - e_{qx}}{T_a e_{qh}} e_h - \frac{1}{e_{qh} T_w} + \frac{f T_w}{T_e} \right) + y \left(\frac{e_{qy} K_P - e_{qx}}{T_a e_{qh}} e_y + \frac{f e_{qy} T_w}{e_{qh} T_e} \right) \end{cases} \quad (20)$$

$$\left\{ \begin{array}{l} \dot{x}_t = \frac{1}{T_a} \left[e_y y + (e_x - e_g - D_a)x_t - \frac{2T_w}{T_e^2} r_2 e_h - K_a \xi_1 + D_a x_s - m_g \right] \\ \dot{y} = - \left[\frac{K_P}{T_a} (e_x - e_g - D_a) + K_I \right] x_t - \frac{K_P}{T_a} \left[e_y y - \frac{2T_w}{T_e^2} r_2 e_h - K_a \xi_1 + D_a x_s - m_g \right] \\ \dot{x}_s = \frac{1}{T_s} \left[D_a B x_t - (D_s + D_a B) x_s + K_a B \xi_1 - \frac{1}{R_g T_g} \xi_2 \right] \\ \dot{\xi}_1 = x_t - x_s \\ \dot{\xi}_2 = x_s - \frac{1}{T_g} \xi_2 \\ \dot{r}_1 = r_2 \\ \dot{r}_2 = -\frac{2}{T_e^2} r_1 - \frac{2f}{T_e} r_2 + e_{qx} x_t + e_{qy} y + e_{qh} h \\ \dot{h} = -\frac{2fT_w}{T_e^3} r_1 - \frac{2T_w}{T_e^2} r_2 \end{array} \right. \quad (21)$$

$$\left\{ \begin{array}{l} \dot{x}_t = \frac{1}{T_a} [e_y y + (e_x - e_g - D_a)x_t + e_h h - K_a \xi_1 + D_a x_s - m_g] \\ \dot{y} = - \left[\frac{K_P}{T_a} (e_x - e_g - D_a) + K_I \right] x_t - \frac{K_P}{T_a} [e_y y + e_h h - K_a \xi_1 + D_a x_s - m_g] \\ \dot{x}_s = \frac{1}{T_s} \left[D_a B x_t - (D_s + D_a B) x_s + K_a B \xi_1 - \frac{1}{R_g T_g} \xi_2 \right] \\ \dot{\xi}_1 = x_t - x_s \\ \dot{\xi}_2 = x_s - \frac{1}{T_g} \xi_2 \\ \dot{r}_1 = r_2 \\ \dot{r}_2 = r_3 \\ \dot{r}_3 = r_4 \\ \dot{r}_4 = -\frac{24}{T_e^4} r_1 - \frac{24f}{T_e^3} r_2 - \frac{12}{T_e^2} r_3 - \frac{4f}{T_e} r_4 + e_{qx} x_t + e_{qy} y + e_{qh} h \\ \dot{h} = -\frac{24fT_w}{T_e^5} r_1 - \frac{24T_w}{T_e^4} r_2 - \frac{12fT_w}{T_e^3} r_3 - \frac{4T_w}{T_e^2} r_4 \end{array} \right. \quad (22)$$

Verification of model

After being connected to the grid, hydroelectric units can employ wicket gate regulation mode, power regulation mode, or frequency regulation mode. The use of frequency regulation mode by hydroelectric units under grid-connected conditions can not only effectively address grid frequency fluctuations and ensure the safe and stable operation of the power system, but also play a key regulatory role in the context of large-scale integration of new energy sources. Therefore, frequency regulation mode is also an important regulation mode for units after grid connection. This paper merely takes frequency regulation mode as an example to study the impact of different pipeline models and operating conditions on the stability of the units. In future research, we will further investigate the stability under other regulation modes, such as power regulation mode.

To verify the correctness and effectiveness of the proposed model defined by Eq. (19), the dynamic response process (DRP) of the models defined by Eq. (19)–(22) are compared with those of the GCHTGS considering the transcendental model of the penstock system. For the GCHTGS system, the load disturbance is chosen as the external disturbance. The values of parameters and the simulation block diagram of the GCHTGS system are shown in Table 3 and Fig. 9.

| HTGS | | | | PG | |
|------------|--------|------------|--------|------------|--------|
| Parameters | Values | Parameters | Values | Parameters | Values |
| H_0 | 45.45 | e_{gh} | 0.5 | B | 0.1 |
| Q_0 | 97.7 | e_{gx} | 0 | D_s | 0.4 |
| T_w | 2 | e_{gy} | 1 | T_s | 40 |
| T_y | 0 | e_g | 0 | R_g | 0.2 |
| K_d | 0 | T_a | 10 | T_g | 40 |
| e_h | 1.5 | K_a | 2 | | |
| e_x | -1 | D_a | 0.073 | | |
| e_y | 1 | bp | 0 | | |

Table 3. Values of parameters of the GCHTGS system.

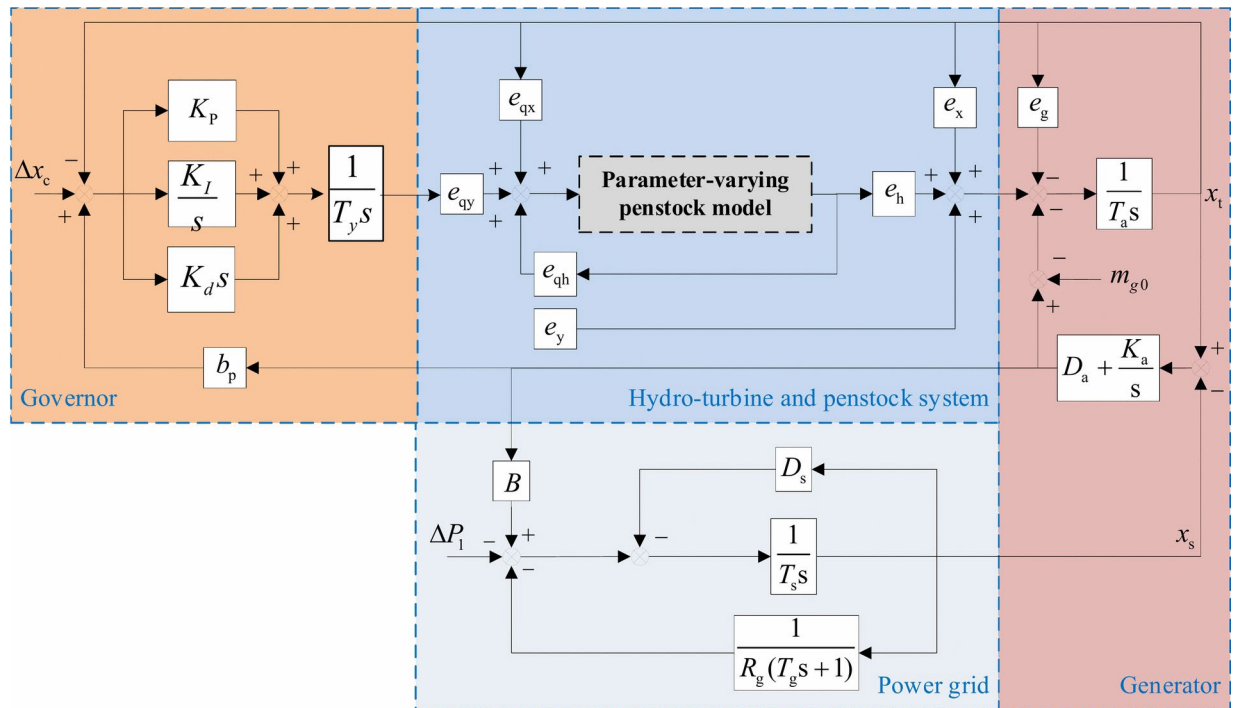


Fig. 9. Block diagram of the GCHTGS.

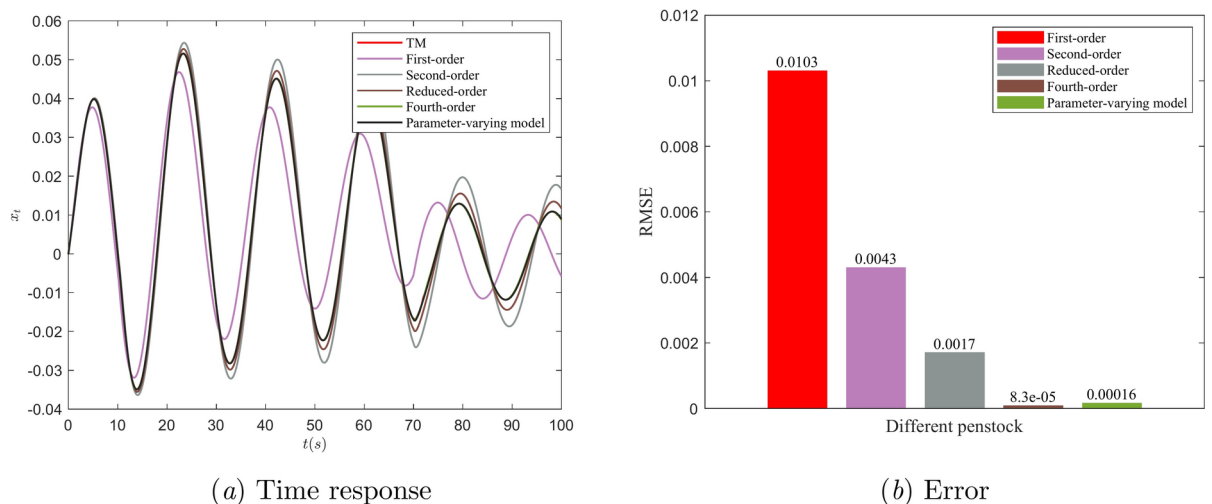


Fig. 10. Comparison of different penstock models, (a) Time response, (b) Error.

The results of DRP of the GCHTGS system considering different penstock models are shown in Fig. 10(a). And the error of different penstock models compared with TM is shown in Fig. 10(b). From Fig. 10, the DRP of the rotational speed of GCHTGS system considering the fourth-order EWHM, PVM and TM models are almost coincident. The results show that the PVM and fourth-order EWHM have greater accuracy. The DRP of second-order EWHM and the reduced-order EWHM have small deviation from TM, especially in the peaks and troughs regions. However, the DRP of first-order RWHM has a large deviation from TM. It is clearly shown that the DRP of first-order RWHM has a different oscillation period compared to the second-order EWHM, reduced-order EWHM, fourth-order EWHM, PVM and TM. The correctness and effectiveness of the proposed PVM for the GCHTGS system are verified.

Stability analysis of GCHTGS

Hopf bifurcation theory

The stability of the GCHTGS is investigated in this paper based on the HBT. The GCHTGS system defined by Eq. (19) can be expressed by state equations $\dot{x} = f(x, \mu)$, where x is the state vector and μ is the bifurcation parameter. The equilibrium point x_E of the state equations can be obtained by setting $\dot{x} = 0$. The Jacobian matrix of the system at the equilibrium point x_E can be obtained as $J(\mu) = Df_x(x_E, \mu)$, whose characteristic equation $\det(J(\mu) - \lambda I) = 0$ is:

$$a_0(\mu)\lambda^n + a_1(\mu)\lambda^{n-1} + \dots + a_{n-2}(\mu)\lambda^2 + a_{n-1}(\mu)\lambda + a_n(\mu) = 0 \quad (23)$$

where $a_i(\mu)$ ($i = 1, 2, \dots, n$) are the coefficients of the characteristic equation and λ are eigenvalues.

The system exists Hopf bifurcation if the following conditions are met²⁷:

$$\left\{ \begin{array}{l} a_i(\mu_c) > 0 (i = 1, 2, \dots, m) \\ \Delta_i(\mu_c) > 0 (i = 1, 2, \dots, m-2), \Delta_{m-1}(\mu_c) = 0 \\ \Delta_j(\mu_c) = \begin{vmatrix} a_1 & 1 & 0 & \cdots & 0 \\ a_3 & a_2 & a_1 & \cdots & 0 \\ a_5 & a_4 & a_3 & \cdots & 0 \\ \vdots & \vdots & \vdots & \ddots & \vdots \\ a_{2j-1} & a_{2j-2} & a_{2j-3} & \cdots & a_j \end{vmatrix} \\ \sigma'(\mu_c) = \text{Re} \left(\frac{d\lambda}{d\mu} \Big|_{\mu=\mu_c} \right) \neq 0 \end{array} \right. \quad (24)$$

Influence of different penstock models on stability

Stability region analysis

The bifurcation line, which consists of all bifurcation points (K_p, K_i) on the K_p - K_i parameter plane, is used to describe the stability of the GCHTGS. The parameter plane, obtained by solving Eq. (24), is divided into three regions: a stability region, a critical stability region, and an unstable region. The stability region is determined using the transversal coefficient $\sigma'(\mu_c)$ and bifurcation line. Figure 11 shows the procedure for calculating the stability region.

The parameters of the GCHTGS are shown in Table 1, where the load disturbance condition is considered. The bifurcation line can be obtained based on the above procedures, as shown in Fig. 12.

Firstly, the stability of the GCHTGS system considering the PVM is analyzed. From Fig. 12(a), the bifurcation line of the PVM initially increases gradually and then decreases rapidly as K_p increases. Based on Fig. 12(b) and the HBT in Section "Hopf bifurcation theory", the GCHTGS' Hopf bifurcation is determined to be supercritical. Consequently, the stability region is located at the lower side of the bifurcation line, while the unstable region is located on the other side.

Then the stability of the GCHTGS system considering different penstock models is investigated. Different penstock models exhibit different stability regions, among which the GCHTGS system with first-order RWHM has the largest stability region and the GCHTGS system with second-order EWHM has the smallest stability region. The stability region of the GCHTGS system with PVM closely matches that of the fourth-order EWHM. The results show that the stability region of the GCHTGS system with RWHM is significantly larger than that with EWHM. For lower-order EWHM, the stability region of the GCHTGS system is smaller than for higher-order EWHM. Compared to the stability region of fourth-order EWHM and PVM, we can conclude that the proposed PVM has the same stability as the fourth-order EWHM. Additionally, the calculation time of stability calculation with different penstock models under a certain operation condition are recorded as 23.91 s, 30.89 s, 55.74 s and 31.84 s.

To further verify the model accuracy of the proposed PVM, the stability regions of the PVM and the fourth-order EWHM with different T_e are shown in Fig. 13. The PVM and the fourth-order EWHM exhibit consistent stability regions under different T_e . Therefore, the proposed PVM achieves high accuracy while maintaining low computational complexity. The comparison of different models is listed in Table 4.

From the experiments above, some important conclusions can be made:

- (1) The original transcendental model of penstock is nonlinear, which is not suitable for stability analysis. Therefore, some approximation models, such as first-order RWHM, second-order EWHM and fourth-order EWHM are used for theoretical stability analysis.
- (2) Among these models, the fourth-order EWHM has the highest model accuracy, as demonstrated by numerical simulation in Sections "Parameter-varying penstock model" and "Verification of model" due to its highest model order. However, it leads to higher computational complexity.
- (3) The accuracy of traditional first-order RWHM and second-order EWHM can't be guaranteed, and their corresponding stability analyses are less accurate compared with the fourth-order EWHM.
- (4) The proposed PVM has higher accuracy than the traditional first-order RWHM and second-order EWHM. It achieves the same stability as the fourth-order EWHM while maintaining lower computational complexity.
- (5) The proposed PVM is the most suitable model for stability analysis of GCHTGS due to its higher accuracy and simpler form, which results in low computational complexity.

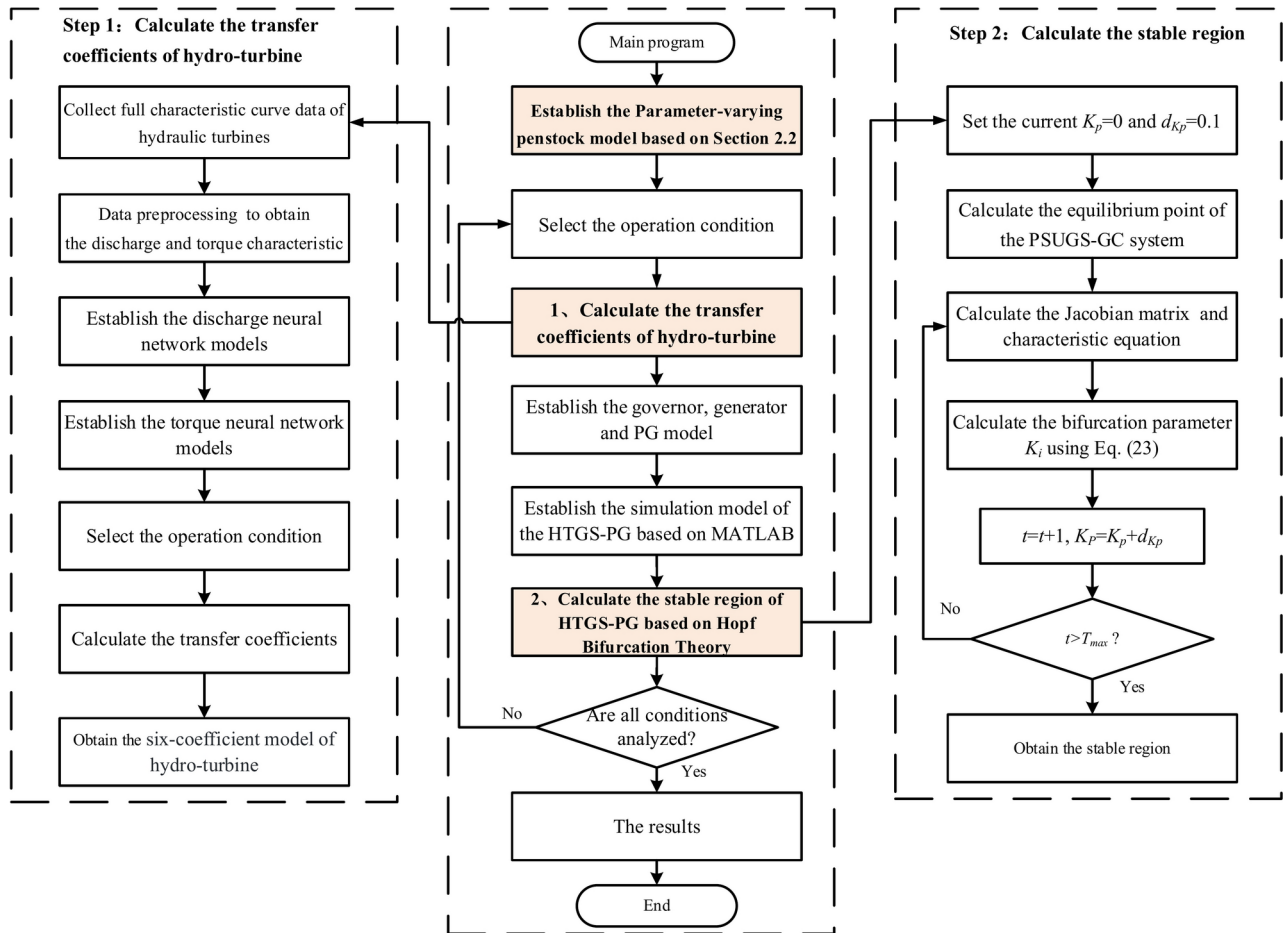


Fig. 11. The process of calculating the stability region.

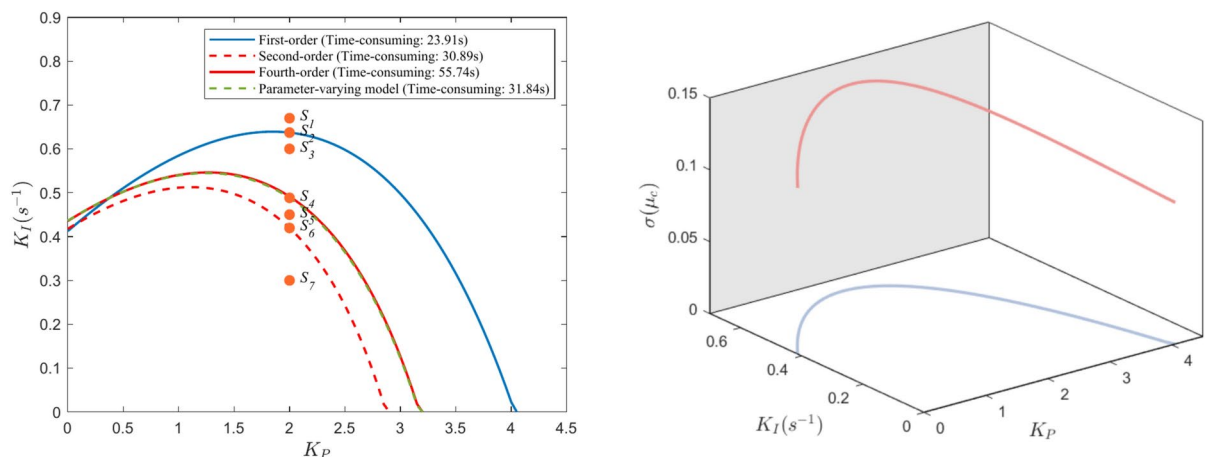


Fig. 12. Stability region and transversal coefficient $\sigma'(\mu_c)$ of the GCHTGS.

Eigenvalue analysis

In this part, the conventional eigenvalue analysis is conducted to explore the influence of penstock models on the stability of GCHTGS. According to classical control theory, a control system is stable if and only if all its eigenvalues have negative real parts.

When $K_i=0.45$, multiple characteristic roots of the characteristic equation (i.e. Equation (23)) are calculated. The trajectories of the eigenvalues as K_p increases are shown in Fig. 14. From Fig. 14(a), the eigenvalues of GCHTGS with different penstock models consist of two complex conjugate pairs and several real eigenvalues.

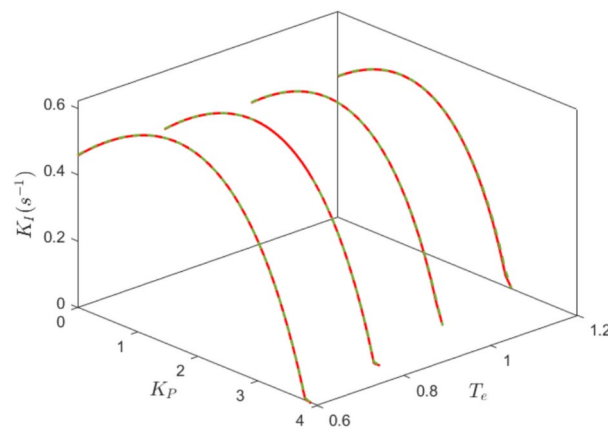


Fig. 13. The stability regions under fourth-order and PVMs with different values of T_e .

| Model | Equations | Characteristics |
|--------------------------|---|--|
| The Transcendental model | $G_{P0}(s) = -\frac{T_w}{T_e} \tanh(T_e s + f)$ | Advantages: High accuracy Disadvantages: It is not suitable for system stability analysis |
| The first-order EWHM | $G_{P1}(s) = -T_w s - \frac{T_w}{T_e} f$ | Advantages: Simple calculation and reasonable accuracy ⁴² Disadvantages: Modeling inaccuracy when penstock length is above 200 m ⁴³ |
| The second-order EWHM | $G_{P2}(s) = -\frac{T_w}{T_e} \frac{f + T_e s}{1 + f T_e s + \frac{1}{2} T_e^2 s^2}$ | Advantages: Second oscillation modes are captured Disadvantages: Modeling inaccuracy ⁴⁴ |
| The fourth-order EWHM | $G_{P3}(s) = -\frac{T_w}{T_e} \frac{f + T_e s + \frac{1}{2} f T_e^2 s^2 + \frac{1}{6} T_e^3 s^3}{1 + f T_e s + \frac{1}{2} T_e^2 s^2 + \frac{1}{6} f T_e^3 s^3 + \frac{1}{24} T_e^4 s^4}$ | Advantages: Higher oscillation modes are captured Disadvantages: Complex calculations ⁴⁵ |
| The proposed model | $G_{P5}(s) = -\frac{T_w}{T_e} \frac{(\frac{2fT_e^2}{\pi^2} s^2 + T_e s + f) w_n^2}{\sigma s^2 + 2\xi w_n s + w_n^2}$ | Advantages: Higher precision and simpler form |

Table 4. Comparison of different penstock models.

Only one pair of conjugate eigenvalues $\lambda_{1,2}$ has a negative real part as the variation of K_p called the dominant eigenvalue. Therefore, the change law of the real part of the dominant eigenvalue with the parameters of K_p is shown in Fig. 14(b). For constant K_p , the real part of the dominant pole first decreases and then increases with K_p , causing the system to transition from stable to unstable and back to stable. When the real parts of the complex conjugate eigenvalues are zeros, the system reaches a critical steady state. Figure 14(f) compares the variation of the dominant eigenvalue's real part for GCHTGS with different penstock models. From Fig. 14(f), we can see that the stable range of the GCHTGS system considering different penstock models is $0.1789 < K_p < 3.1582$, $0.2259 < K_p < 1.8563$, $0.0872 < K_p < 2.2143$ and $0.0945 < K_p < 2.2116$. The first-order penstock model yields the largest stable range, the second-order model the smallest, and the fourth-order model and PVM exhibit similar stable ranges, consistent with previous stability analysis.

Numerical simulation and verification of stability

To verify the correctness of the above analysis results and investigate the dynamic characteristics of the GCHTGS system under different controller parameter values, seven state points $S_1, S_2, S_3, S_4, S_5, S_6$ and S_7 are chosen in Fig. 7(a) as the representatives for numerical simulation.

The Runge–Kutta method embedded in MATLAB is used for numerical simulation, and the DRP and the corresponding phase space trajectories are shown in Fig. 15.

From Fig. 15, we can observe the following:

- (1) The numerical simulation results agree with the HBT analysis. The DRP and phase space trajectories of state variables in the stability region exhibit damped oscillations and eventually converge to the equilibrium point. In the critical region, the DRP gradually transitions into a state of sustained oscillation with a consistent amplitude after multiple oscillation cycles, and the phase space trajectory converges to the limit cycle. In the unstable region, the DRP exhibits divergent oscillations, and the phase space trajectory gradually diverges.
- (2) For S_1 , compared with other models, the divergence speed of DRP of GCHTGS with the second-order EWHM is faster. The divergence speed of the GCHTGS system considering the fourth-order EWHM and PVM is almost coincident. For S_7 , the divergence speed of DRP of GCHTGS with the first-order EWHM is the fastest, while that with the second-order EWHM is the slowest.
- (3) The DRP's divergence speed increases with distance from the bifurcation line for state points in the unstable region. On the other hand, the dynamic response's convergence speed increases with distance from the

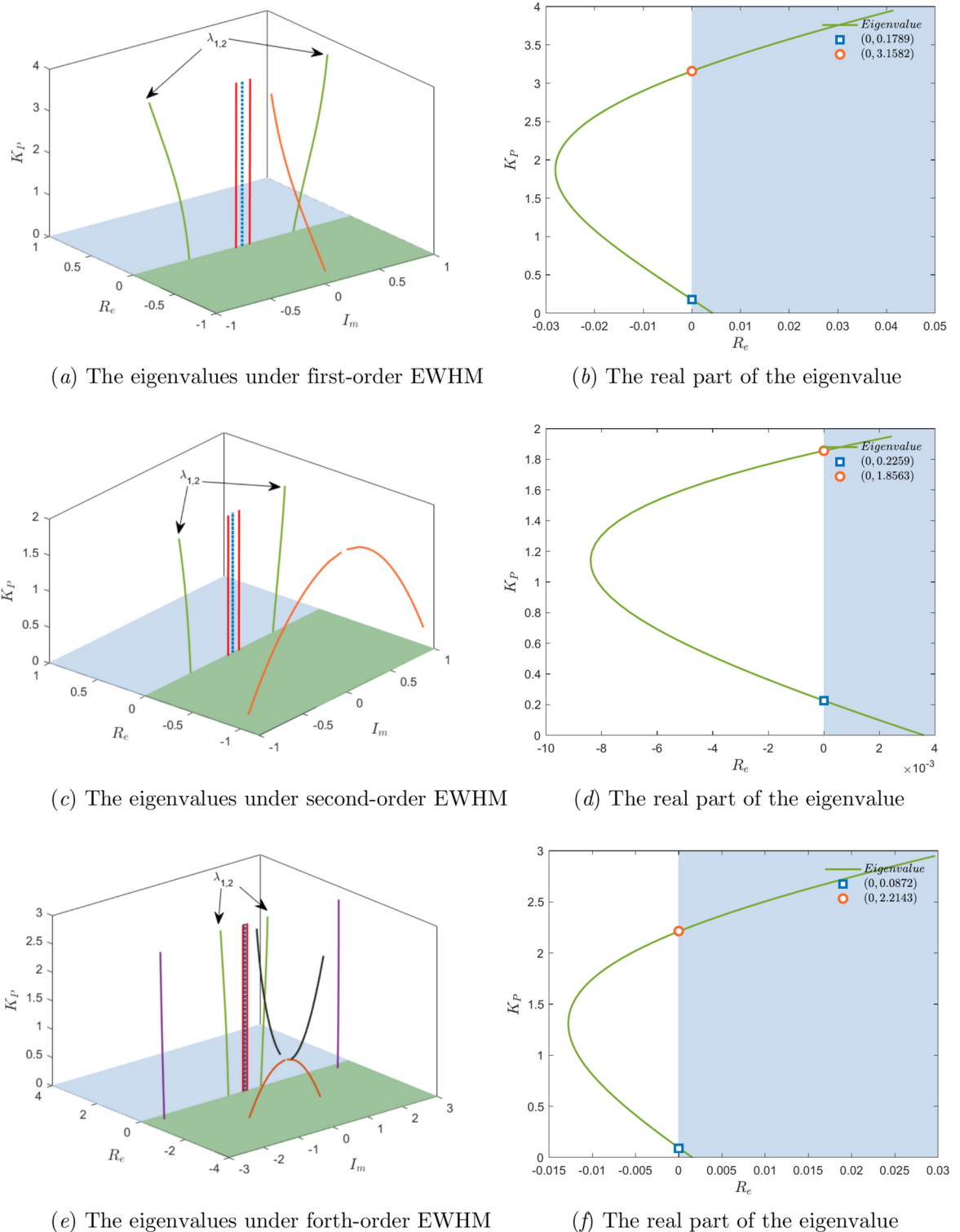


Fig. 14. Changing tracks of the eigenvalue with the bifurcation parameter K_p in Hopf bifurcation.

bifurcation line for state points inside the stability region. Consequently, the stability in the stability region will increase with distance from the bifurcation line, while the stability in the unstable region will decrease.

Stability analysis of GCHTGS under FOC

This section investigates the influence mechanism of the hydro-turbine operating conditions on the stability. The operating conditions of the hydro-turbine mainly depend on the GVO and water head. For a specific hydro-turbine, based on the operational data of the hydropower station, the water head ranges from 155 to 215 m,

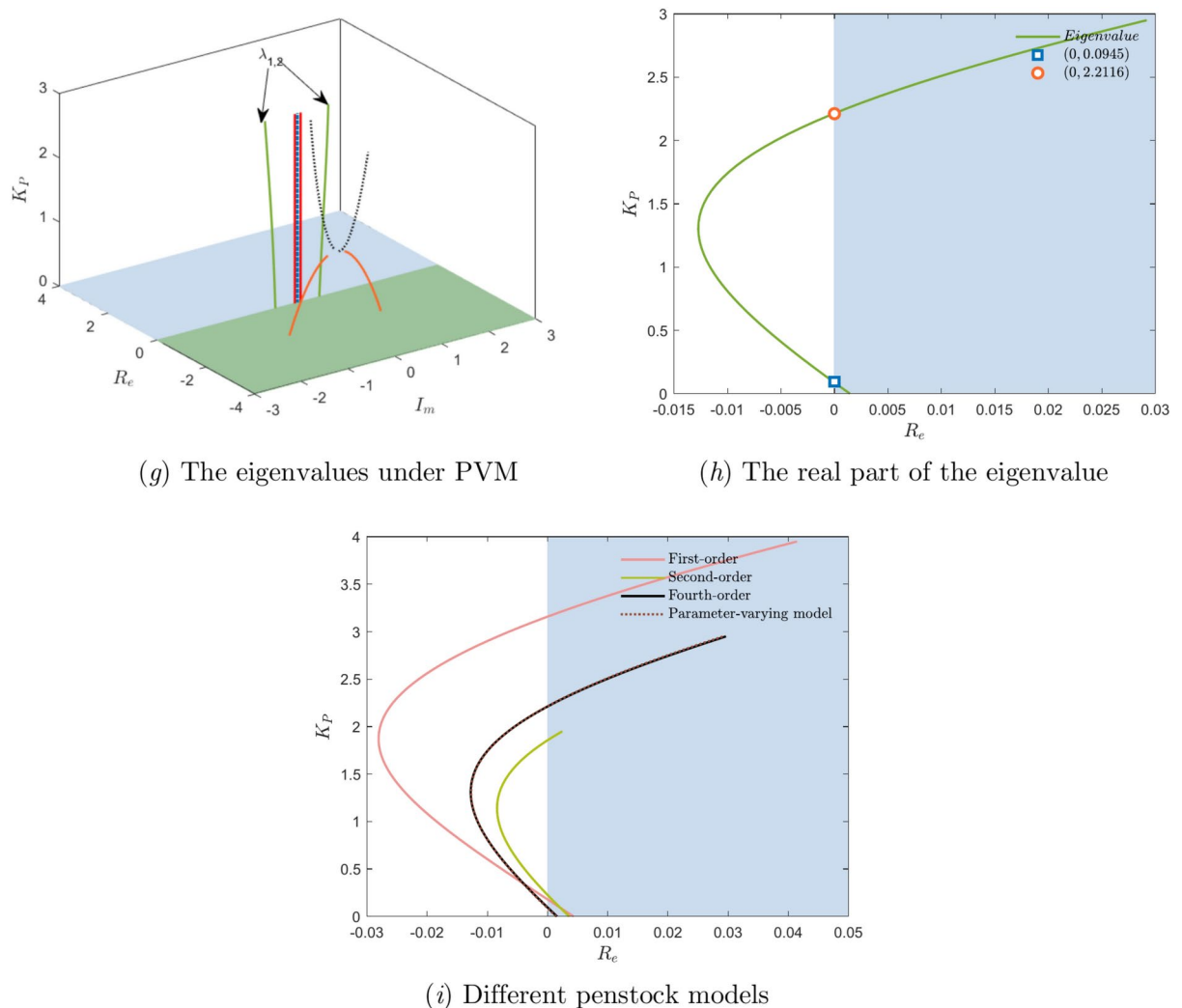
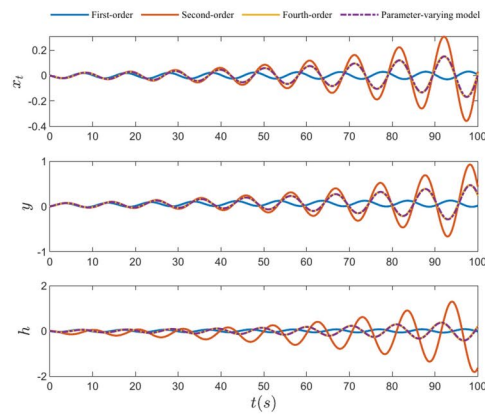
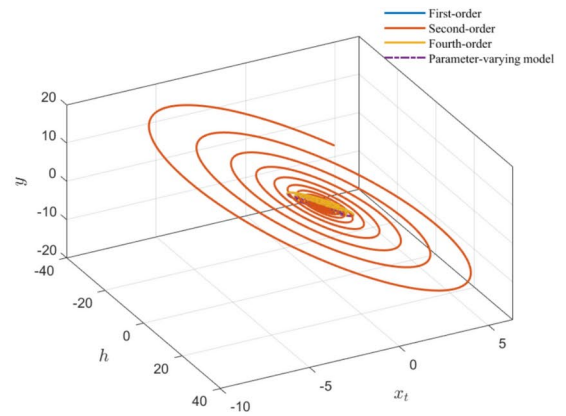


Figure 14. (continued)

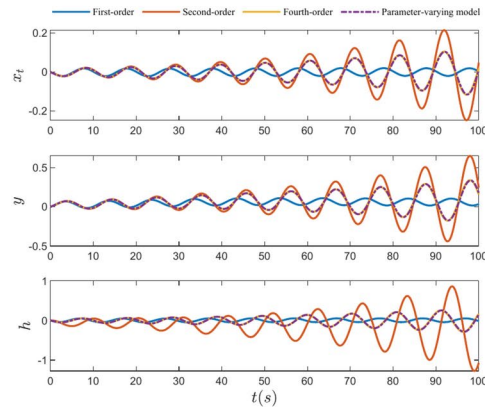
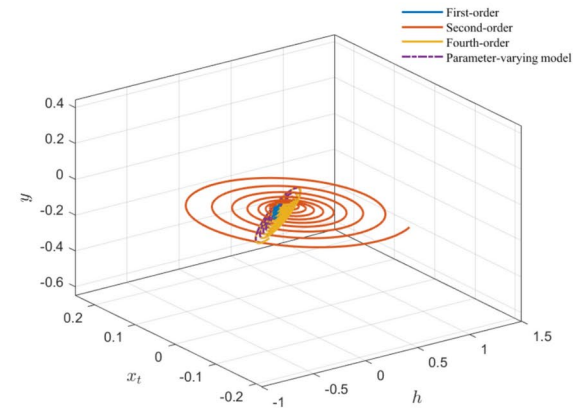
and the GVO varies from 30 to 100%. To facilitate research, it is recommended to select a new operating point for every 10 m change in water head and every 10% interval in GVO. Under different operating conditions, the hydro-turbine has six different transfer coefficients. A total of 64 sets of these six parameters correspond to 64 operating conditions, as shown in Fig. 16.

The K_p - K_i stability region ($K_d = 0$) of the GCHTGS under FOC is calculated using HBT, and the corresponding stability region area is shown in Table 5 and Fig. 17. Based on different colors, the operating conditions can be categorized into four distinct regions. The operating conditions in the first column of the table belong to the first region, characterized by the deepest color. The area of the stability region exceeds 9, which is more than twice that of other operating conditions, indicating the strongest system stability. The second column of the table represents the second region, where the stability region area ranges from 4.2 to 6.9. The intensity of color (i.e., stability) lies between the adjacent columns. The blue segments in columns 4 to 7 of the table represent the third region, with relatively smaller stability region areas, all below 2, indicating comparatively weaker system stability in this region. The remaining operating conditions in the table represent the fourth region, with stability region areas ranging from 2 to 3.3.

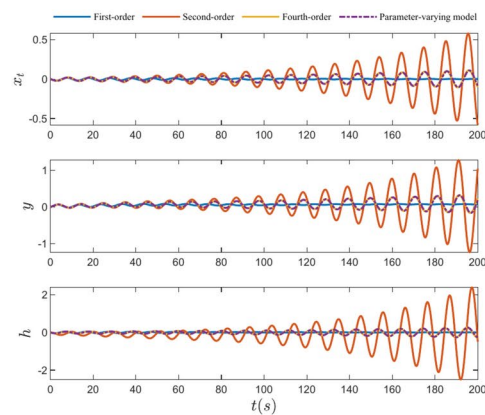
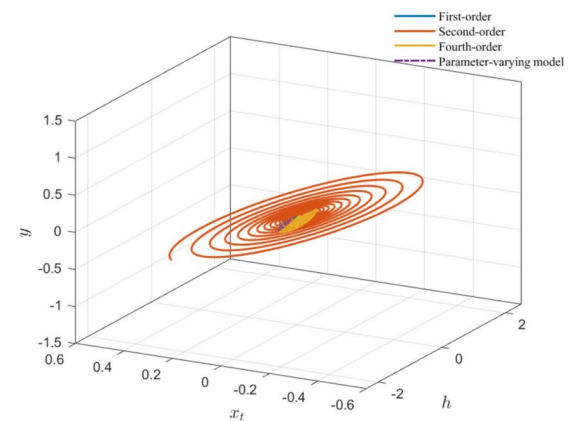
To further investigate the relationship between system stability, GVO and water head, the variation of the stability region area with water head under different GVOs is illustrated in Fig. 18 (a). The bar chart in Fig. 18 (b) illustrates the stability region area of the system at different water heads when the GVO is 60%. As shown in Table 4 and Fig. 18, under different GVOs, the stability region area gradually decreases with increasing water head, approximating a linear relationship. Among the same GVOs, the condition with a water head of 155 m has the largest stability region. The variation of the stability region area with GVO under different water heads is depicted in Fig. 19 (a). The bar chart in Fig. 19 (b) represents the stability region area of the system at a water head of 185 m with different GVOs. In contrast to the previous scenario, as the GVO increases, the stability region area initially decreases sharply and then slowly increases. The minimum value for the stability region area occurs around a GVO of 60%–70%. At a given water head, the GVO of 30% corresponds to the largest stability region area.

(a) The DRP of GCHTGS under S_1 

(b) The phase space trajectory

(c) The DRP of GCHTGS under S_2 

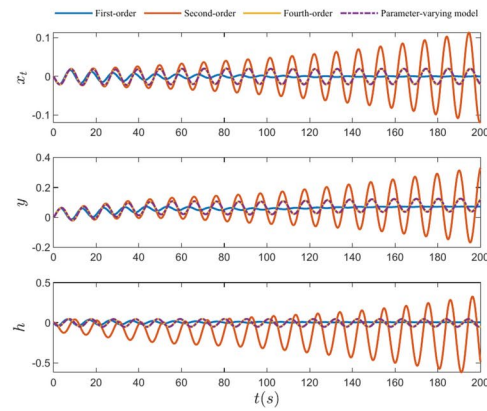
(d) The phase space trajectory

(e) The DRP of GCHTGS under S_3 

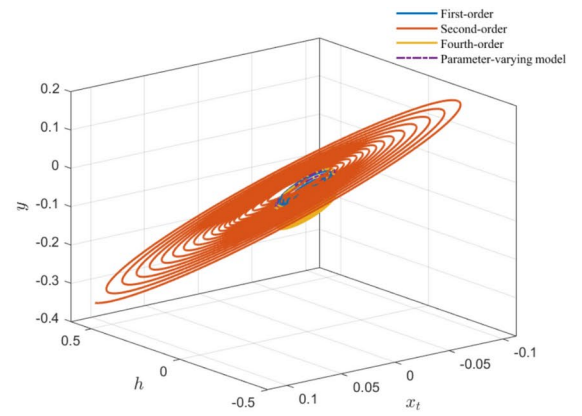
(f) The phase space trajectory

Fig. 15. DRP of characteristic variables x_p , y and h under seven state points and corresponding phase space trajectory of state variables.

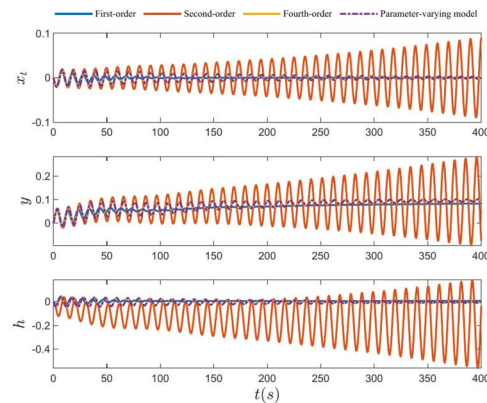
The trajectory of the centroid movement of the stability region under FOC is illustrated in Fig. 20. From Fig. 20(a), it can be observed that at different water heads, as the GVO increases, the centroid first approaches the origin and then gradually moves away, indicating a trend of deteriorating and then improving system stability. Additionally, it can be seen from Fig. 20(b) that with an increase in water head, the centroid moves towards the origin, leading to a gradual decrease in system stability. Based on the above analysis, it is discovered that the interaction between GVO and water head results in changes in the stability region.



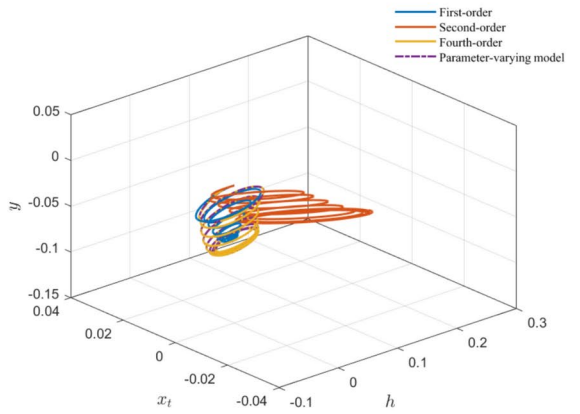
(g) The DRP of GCHTGS under S_4



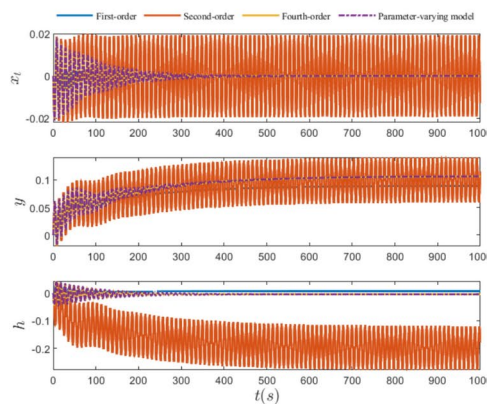
(h) The phase space trajectory



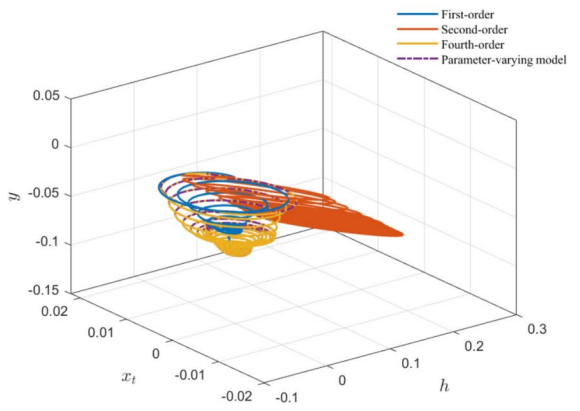
(i) The DRP of GCHTGS under S_5



(j) The phase space trajectory



(k) The DRP of GCHTGS under S_6

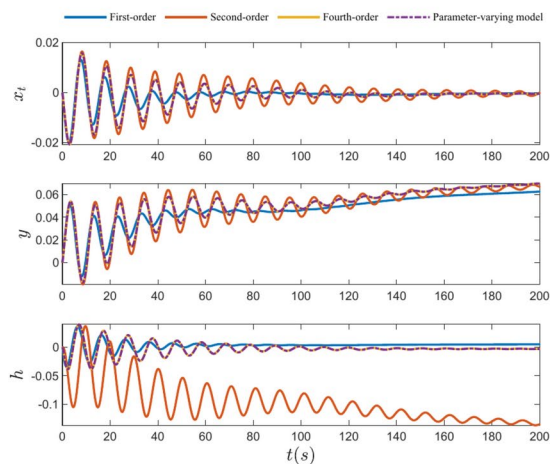
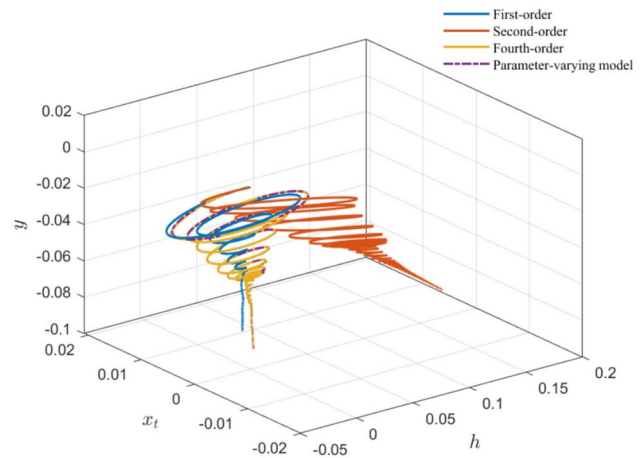


(l) The phase space trajectory

Figure 15. (continued)

Sensitivity analysis

This section examines the impact of system parameters on stability and DRP using both local and global parameter sensitivity analyses. These analyses are employed to quantify the impact of individual input parameters and the interactions between input variables.

(l) The DRP of GCHTGS under S_7 

(m) The phase space trajectory

Figure 15. (continued)

Local sensitivity analysis

This section examines the mechanism by which single parameter variations affects the stability of the system and its DRP. For the important system parameters of GCHTGS, namely, T_a , T_w , B , T_g , D_g , R_g and T_s , these are the influence parameters. The load disturbance experiment is carried out while the GCHTGS is under rated operating conditions ($H=195$ m, $Y=80\%$). Different values within a reasonable range are adopted for each influencing parameter. Then, the corresponding stability region of the GCHTGS is determined based on the HBT in Section "Stability analysis of GCHTGS". A particular state point within the stability region is selected to calculate the DRP, as shown in Figs. 21, 22, 23, 24, 25, 26, 27, where a state point (1.0, 0.1) is chosen for simulation. From Figs. 21, 22, 23, 24, 25, 26, 27, the following conclusions can be drawn:

- (1) Both T_a and T_w have a significant impact on the stability and DRP of the system, where T_w has a greater degree of influence. However, the influence laws of T_a and T_w are opposite. As T_a gradually increases, the stability region of the system also increases, while the oscillation amplitude of the DRP of x_t gradually decreases and the oscillation period gradually increases. In contrast, as T_w gradually increases, the stability region of the system significantly decreases, the oscillation amplitude of the DRP of x_t gradually increases, and the oscillation period remains unchanged.
- (2) B has a slight influence on the stability of the system. As B gradually increases, the K_p coordinate axis contracts to the left, the K_I coordinate axis expands upward, and the stable range of the system slightly increases. As shown in Fig. 26(b), B has a significant impact on the DRP of the system. As B gradually increases, the oscillation amplitude of the DRP of x_t gradually increases.
- (3) T_g , D_g , R_g and T_s have no impact on the stability of the system, but they have a significant influence on the DRP of the system. As T_g , D_g , R_g and T_s gradually increase, the stability region of the system remains unchanged. As T_g and R_g gradually increase, the oscillation amplitude of the DRP of x_t gradually increases. Conversely, as D_g and T_s gradually increase, the oscillation amplitude of the DRP of x_t gradually decreases.

Global sensitivity analysis

Based on the local sensitivity analysis method, a qualitative analysis of the influence of individual parameter changes on system stability and DRP has been conducted. To further quantitatively analyze the influence of parameter changes on system stability and DRP and explore the coupling effects among parameters, the Sobol index method (SIM) is adopted for global sensitivity analysis of system parameters⁴⁶. The main effect index S_1 , total effect index S_T and interaction effect index S_{inter} for the parameters can be obtained based on the SIM.

The S_1 denotes the influence of an independent parameter on the system output. A higher value indicates a stronger impact of that parameter on the output. The S_T considers the main effects of the parameters themselves and the interaction effects with other parameters. The S_{inter} for a certain parameter represents the degree to which it affects the model's output when interacting with other parameters. Specifically, the second-order interaction effect index S_2 represents the coupling impact of two input variables on the output variable.

(1) Stability analysis

First, the SIM is used for parameter sensitivity analysis on stability under rated operating condition. The obtained S_1 and S_T are shown in Fig. 28. From Fig. 28, the S_1 and S_T show that both T_w and T_a have a significant impact on the stability of the system. Moreover, it can be observed that the independent impact of T_w accounts for 85.5%, while the independent impact of T_a accounts for 10.67%. The coupling impact of other parameters only accounts for 4%. This experimental result is consistent with the local sensitivity analysis results mentioned in Sect. "Local sensitivity analysis".

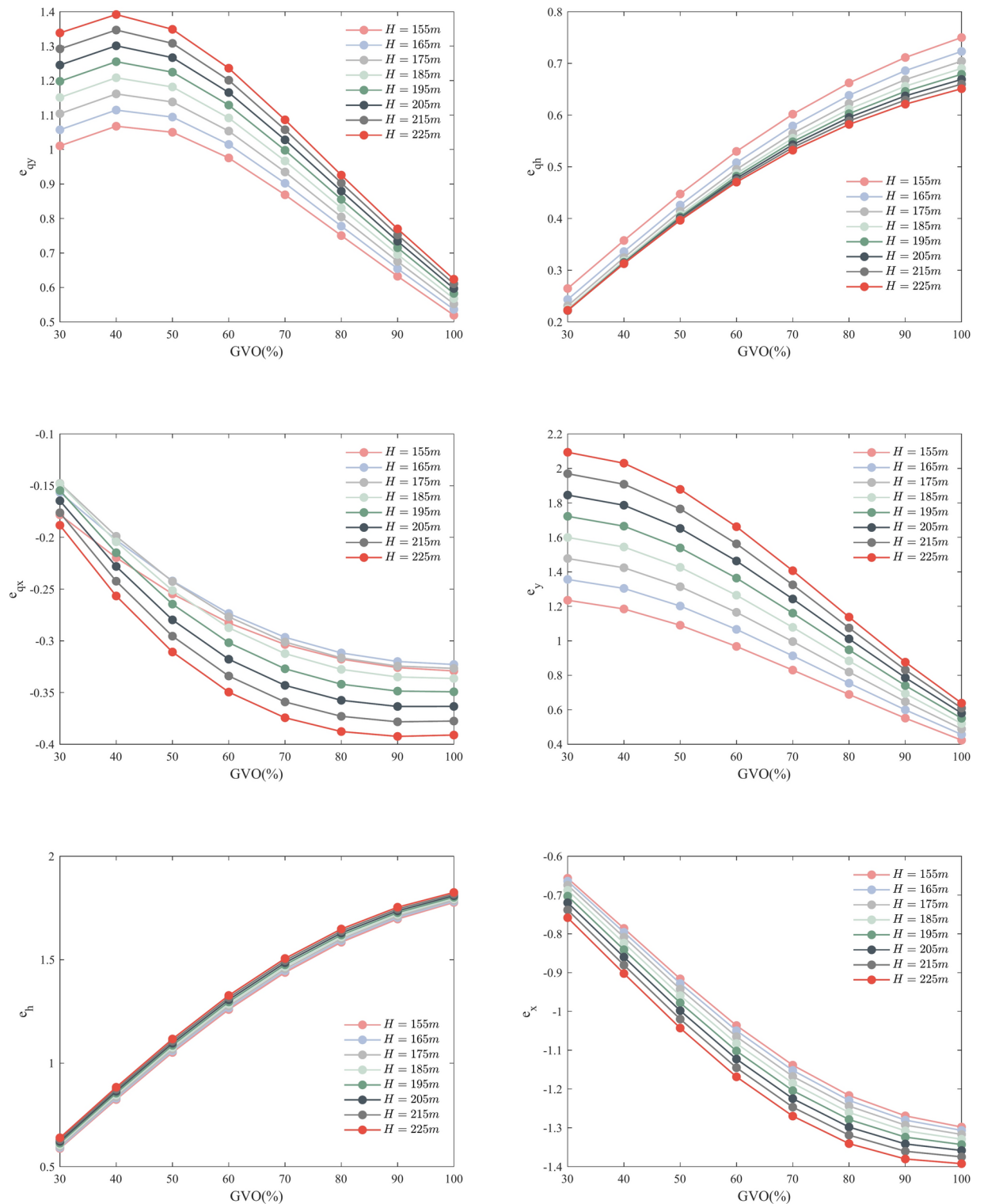


Fig. 16. Six transfer coefficients of the hydro-turbine under FOC.

Then, the S_1 of T_w and T_a under different operating conditions are shown in Fig. 29. From Fig. 29, it can be seen that as the GVO increases under different water heads, the independent impact of T_a on system stability gradually increases, while the independent impact of T_w on system stability gradually decreases. Under different GVOs, as the water head continues to increase, the independent impact of T_a on system stability shows a decreasing trend, while the independent impact of T_w on system stability shows an increasing trend.

The coupling impact index S_2 of T_w and T_a on the system's stability is shown in Fig. 30. It can be observed that the coupling impact indicators of T_w and T_a are negative, indicating that T_w and T_a have opposite effects on

| Area | | GVO (%) | | | | | | | |
|----------------|-----|---------|--------|--------|--------|--------|--------|--------|--------|
| | | 30 | 40 | 50 | 60 | 70 | 80 | 90 | 100 |
| Water head (m) | 155 | 20.0663 | 6.9816 | 3.3757 | 2.224 | 1.8844 | 1.9038 | 2.1599 | 2.6842 |
| | 165 | 16.6837 | 6.3364 | 3.2248 | 2.176 | 1.855 | 1.8652 | 2.0972 | 2.577 |
| | 175 | 14.4963 | 5.8478 | 3.0854 | 2.1192 | 1.8137 | 1.8169 | 2.0249 | 2.4624 |
| | 185 | 12.9574 | 5.4563 | 2.9563 | 2.0577 | 1.7664 | 1.7627 | 1.9508 | 2.3481 |
| | 195 | 11.7794 | 5.1169 | 2.8304 | 1.9934 | 1.7169 | 1.7084 | 1.8766 | 2.2375 |
| | 205 | 10.8058 | 4.8105 | 2.7082 | 1.9274 | 1.6654 | 1.6535 | 1.8045 | 2.1333 |
| | 215 | 9.9569 | 4.5239 | 2.5886 | 1.8604 | 1.613 | 1.5994 | 1.737 | 2.0367 |
| | 225 | 9.1882 | 4.2505 | 2.4704 | 1.7931 | 1.5625 | 1.5486 | 1.674 | 1.9482 |

Table 5. Area of stability region under FOC.

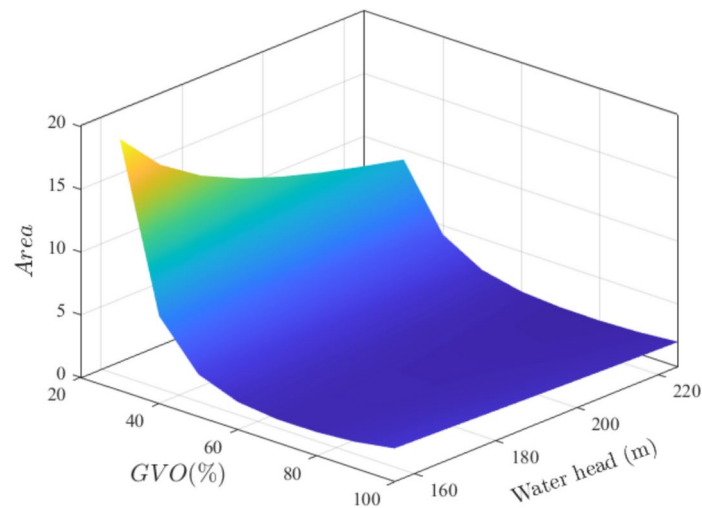


Fig. 17. Area of stability region under FOC.

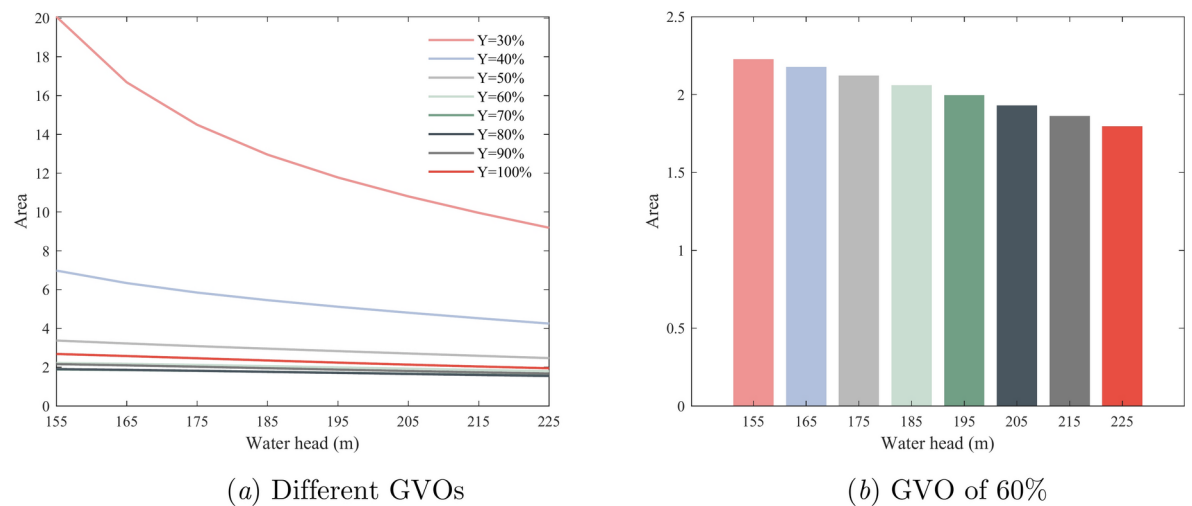
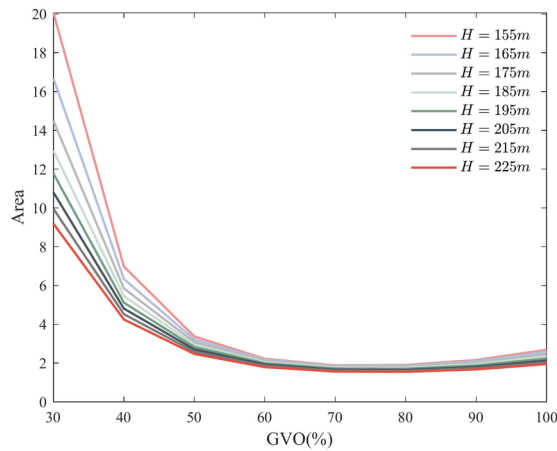
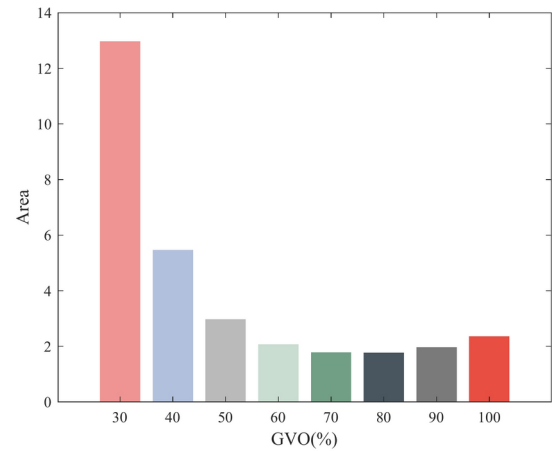


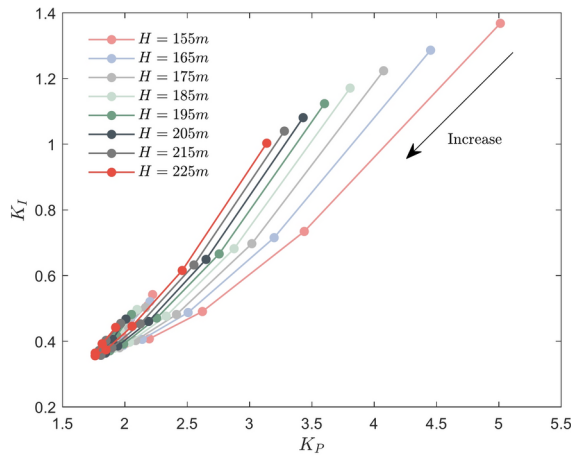
Fig. 18. Area of stability region under FOC.



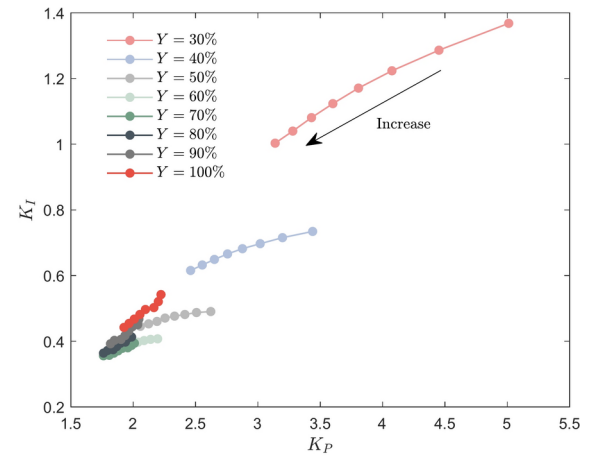
(a) Different water heads



(b) Water head of 185m

Fig. 19. Area of stability region under FOC.

(a) From the perspective of the GVO



(b) From the perspective of the water head

Fig. 20. Changing law of the centroid of the stability region under FOC.

system stability. T_w has a negative impact on the system stability, while T_a has a positive impact. The operating conditions have a slight impact on the coupling impact index S_2 .

(2) Dynamic characteristic analysis

The global parameter sensitivity analysis of the dynamic characteristics of the GCHTGS is carried out in this part. The DRP of x_t under the ideal hydro-turbine model is considered as the reference output. The root mean square error (RMSE) between the DRP under different operating conditions and the reference output is selected as the sensitivity output. The influence of the critical parameters of GCHTGS on RMSE is studied based on the SIM.

The obtained S_1 and S_T under rated operating conditions are shown in Fig. 31. The S_1 of different system parameters are 0.0068, 0.0098, 0.6519, 0.1402, 0.1350, 0.0069 and 0.0183. The S_T are 0.0259, 0.0062, 0.6466, 0.1223, 0.1486, 0.0007 and 0.0212. The interaction effect index S_{inter} are 0.01910, 0.0036, -0.0053, -0.0179, 0.0136, -0.0062 and 0.0029. Based on the above experimental results, it can be concluded that the ranking of the main effect indicator S_1 for the sensitivity of the system parameters on the DPR of x_t is as follows: $B > D_s > R_g > T_g > T_a > T_s > T_w$. The ranking of S_T for the sensitivity of the system parameters on the DPR of x_t is as follows: $B > R_g > D_s > T_w > T_a > T_s > T_g$. Whether it is the main effect index or the total effect index, B has the highest sensitivity to the DPR of x_t , and the independent impact of B accounts for 65.19%. From the interaction effect index S_{inter} , it can be seen that the S_{inter} of T_w , T_a , R_g and T_g are positive, while those of B , D_s and R_g are

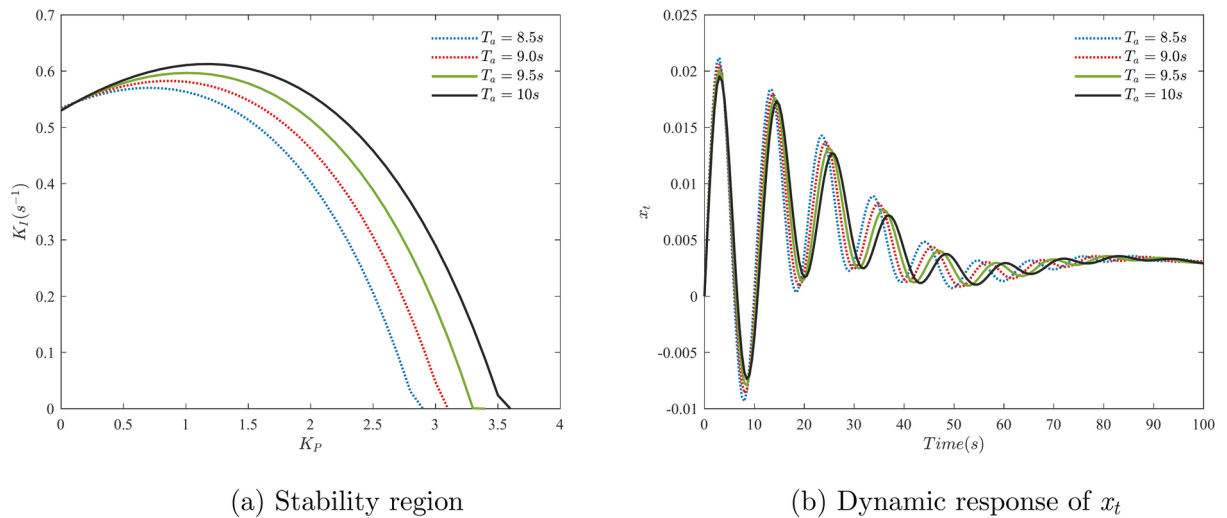


Fig. 21. Influence of T_a on stability and DRP.

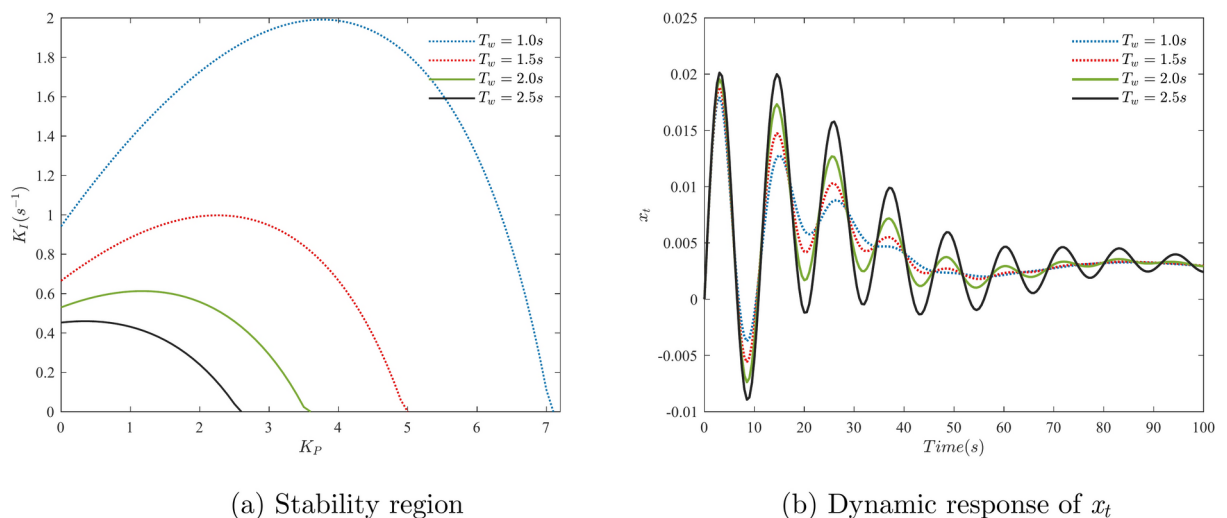


Fig. 22. Influence of T_w on stability and DRP.

negative values. The T_w has the biggest interaction effect index S_{inter} , which indicates that the interactive effect between this parameter and other parameters has a important impact on the DRP.

The second-order interaction effect index S_2 of different parameters is shown in Fig. 32, which representing the coupling impact of between two variables on the dynamic characteristics. The results show that the pairs (B , T_w) and (T_s , R_g) have higher coupling impact on the dynamic characteristics.

The main effect indicator S_1 of different system parameters under different operating conditions is shown in Fig. 33. The main effect indicator of each parameter changes with the variation of operating conditions.

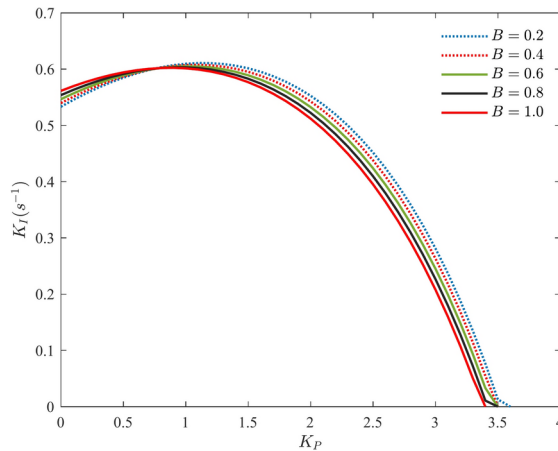
T_w , T_a and T_g have similar variation characteristics. As the GVO increases, S_1 initially increases and then decreases. As the operating head increases continuously, S_1 gradually increases. Under high water heads and a GVO of 70%, T_w , T_a and T_g have a critical impact on the DRP.

For B , as the GVO increases, S_1 first increases and then decreases. When the GVO is 30%, S_1 remains unchanged under various water heads. However, for GVO ranging from 40 to 100%, S_1 decreases slowly with an increasing water head. Under GVO of 30% and 100%, B has a greater impact on the dynamic characteristics of the system.

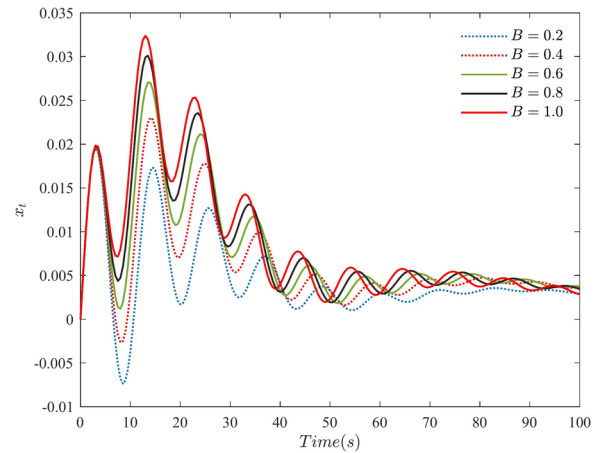
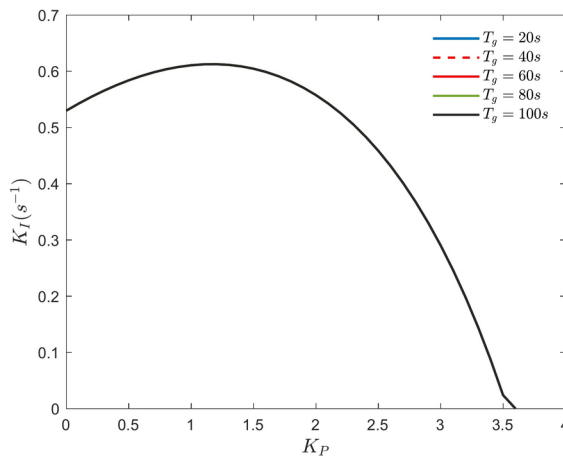
For D_s , as the GVO increases, S_1 gradually decreases. The water head has a slight impact on the dynamic characteristics of the system. Under a GVO of 30%, D_s has an important impact on the DRP.

For R_g , as the GVO increases, S_1 gradually increases. As the operating water head increases, S_1 gradually decreases. Therefore, R_g has an important impact on the DRP under low water heads and large GVO.

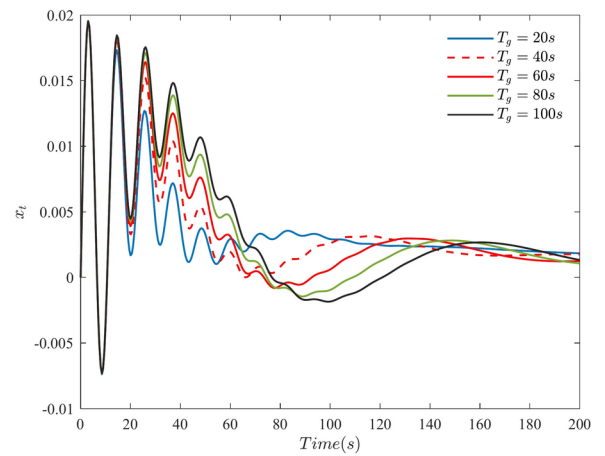
For T_s , as the GVO increases, S_1 gradually decreases. As the water head increases, S_1 gradually increases. Therefore, T_s has an important impact on the DRP under high water heads and small GVO.



(a) Stability region


(b) Dynamic response of x_t
Fig. 23. Influence of B on stability and DRP.


(a) Stability region

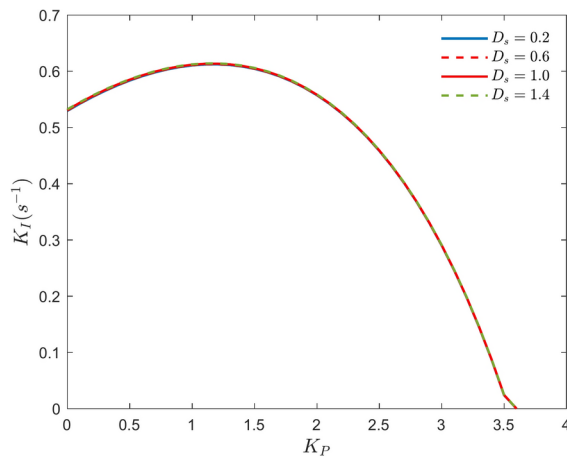

(b) Dynamic response of x_t
Fig. 24. Influence of T_g on stability and DRP.

Conclusions and future research directions

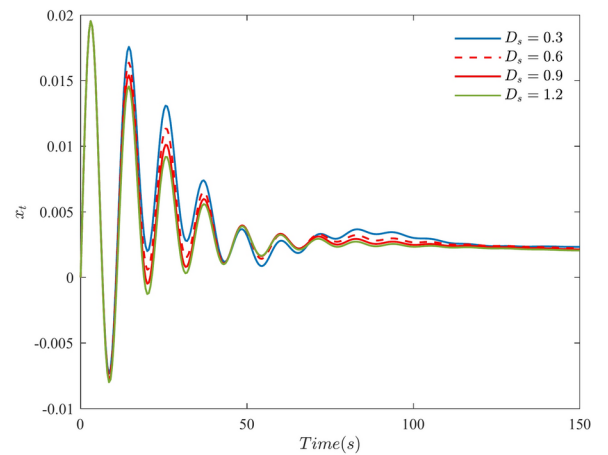
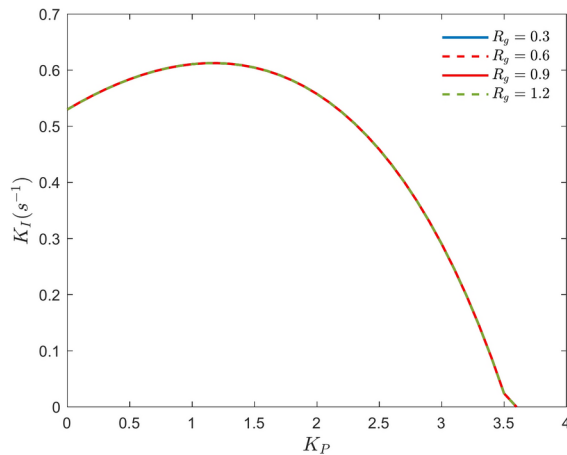
Some conclusions can be drawn as follows:

- (1) Considering the head loss and water elasticity, a PVM for the penstock system is proposed. The effect of the simplification of different penstock models on system response and stability is analyzed from the hydraulic-mechanical perspective, and the experimental results show that the proposed PVM has higher precision and a simpler form than traditional models.
- (2) This paper thoroughly examines and analyzes the impact of hydro-turbine nonlinearity on the stability of GCHTGS. An accurate nonlinear model of the hydro-turbine is established using the BPNN. Considering that the operational point changes frequently, variable transfer coefficients that vary with the GVO and head are used to describe the nonlinear properties of the hydro-turbine. The stability variation mechanism of the GCHTGS under full operating conditions has been revealed.
- (3) The global sensitivity analysis method is adopted to conduct the parameter sensitivity analysis of the GCHTGS. The sensitivity of a single parameter and the coupling effect between parameters are accurately quantified and analyzed for the first time. The relevant conclusions can be applied to the same type of power stations, which are important for optimal unit operation.

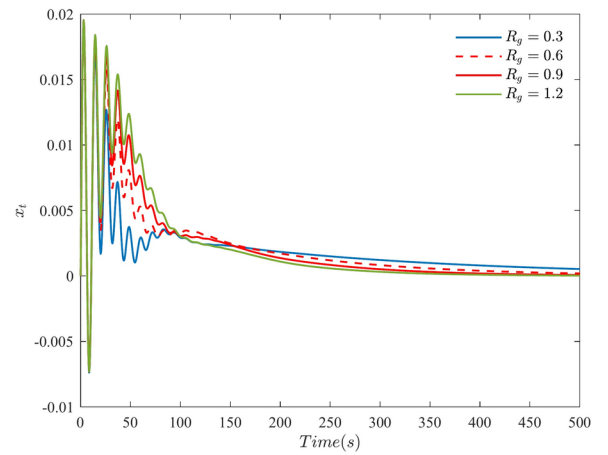
The future research directions are discussed here:



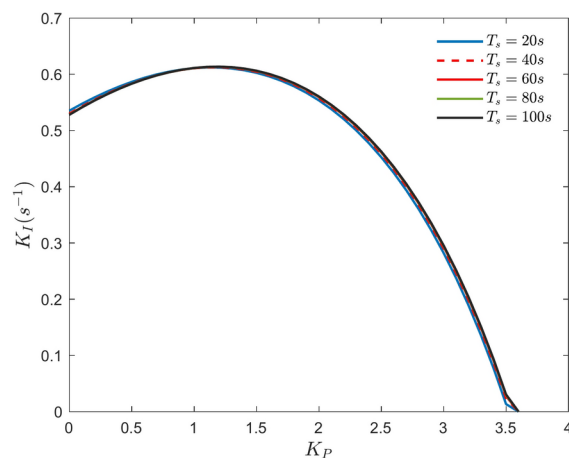
(a) Stability region

(b) Dynamic response of x_t **Fig. 25.** Influence of D_s on stability and DRP.

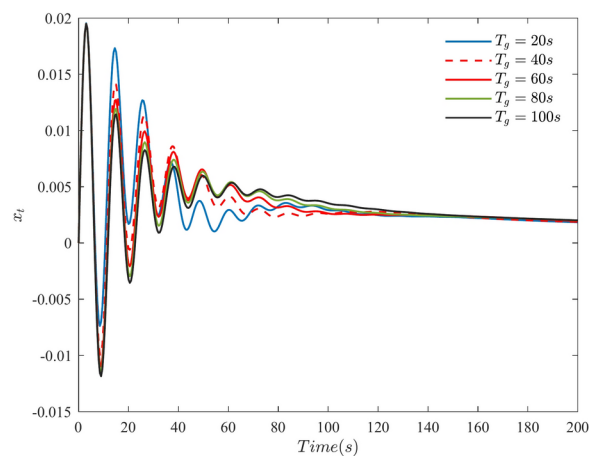
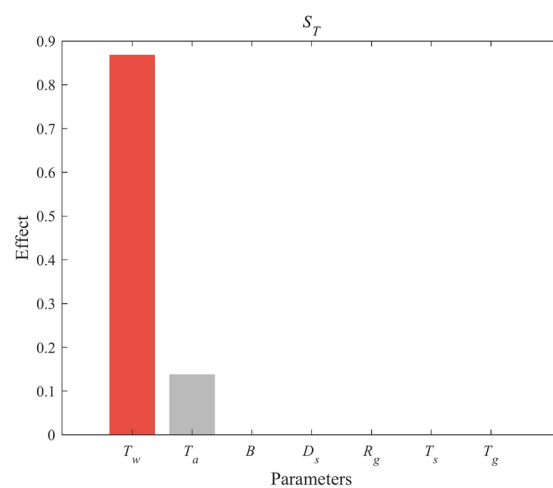
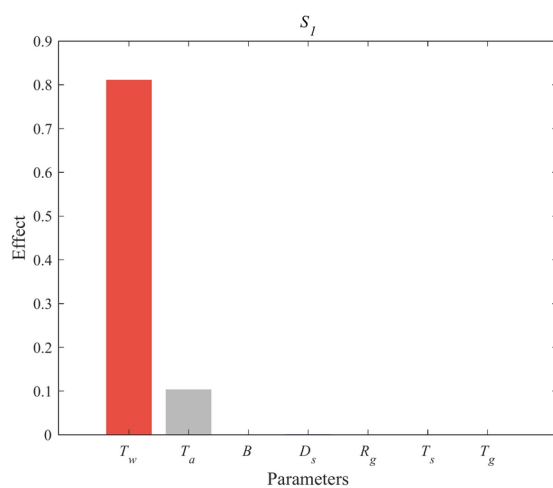
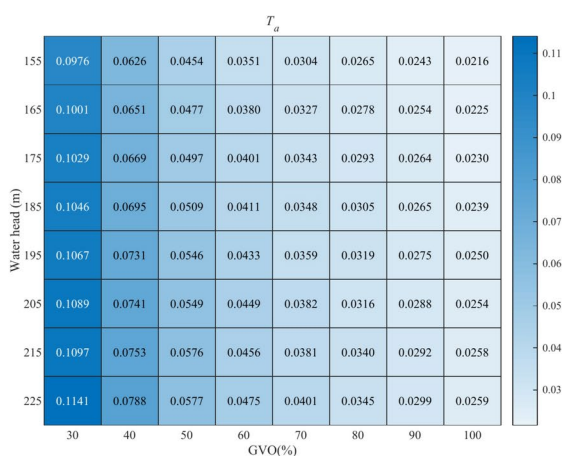
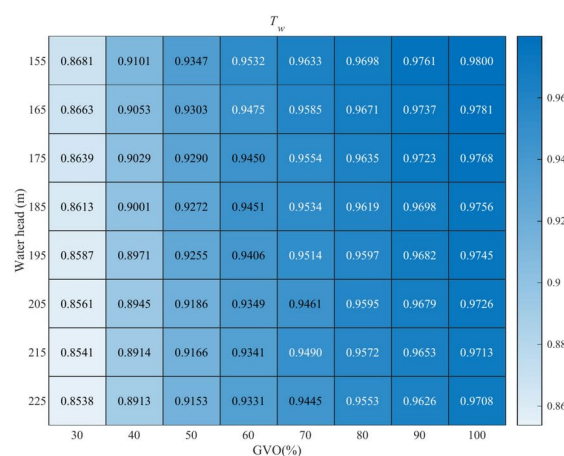
(a) Stability region

(b) Dynamic response of x_t **Fig. 26.** Influence of R_g on stability and DRP.

- (1) Hydropower plants can effectively balance the variability of intermittent renewable energy sources and enhance the regulation quality of the power grid. Due to their unique advantages, hybrid energy systems that incorporate hydropower, photovoltaic power, and wind power are gradually gaining widespread attention. The introduction of photovoltaic power, wind power, and other power electronic devices has made hybrid energy systems more complex. Therefore, the stability of hybrid energy systems and the operational control are important research topics for the future.
- (2) The hydroelectric unit governor system model established in this paper only considers a single pipeline and a single unit model, and does not take into account a complex water conveyance system involving multiple units, multiple pipelines, and components such as surge chambers. Additionally, the established model omits certain governor parameters such as b_p and T_y . Therefore, a more accurate governor model and a hydroelectric unit governor system model incorporating a complex water conveyance system should be considered, and their stability should be investigated. Furthermore, to simplify the study, this paper only conducts stability analysis of the hydroelectric unit under frequency control mode. The stability analysis of the hydroelectric unit under power control mode is worthy of further research in the future.



(a) Stability region

(b) Dynamic response of x_t **Fig. 27.** Influence of T_s on stability and DRP.**Fig. 28.** Dynamic response S_I under rated operating conditions.**Fig. 29.** S_I under FOC.

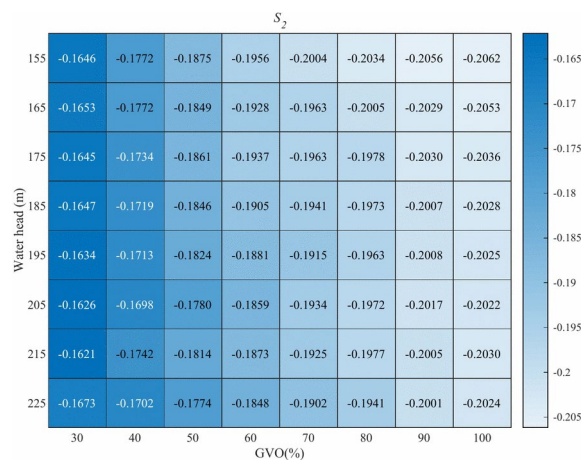


Fig. 30. S_2 under FOC.

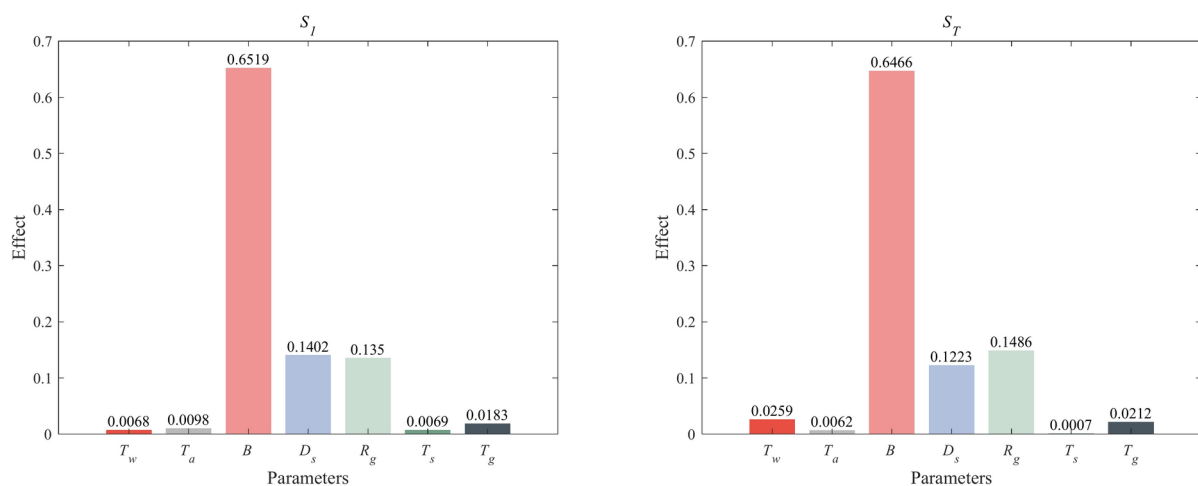


Fig. 31. S_1 under rated operating conditions.

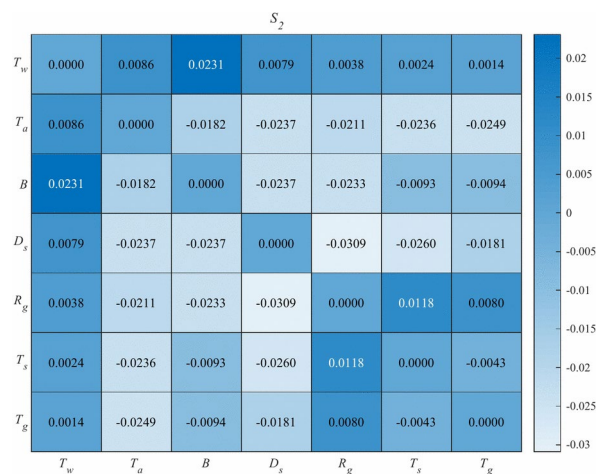


Fig. 32. S_2 under rated operating conditions.

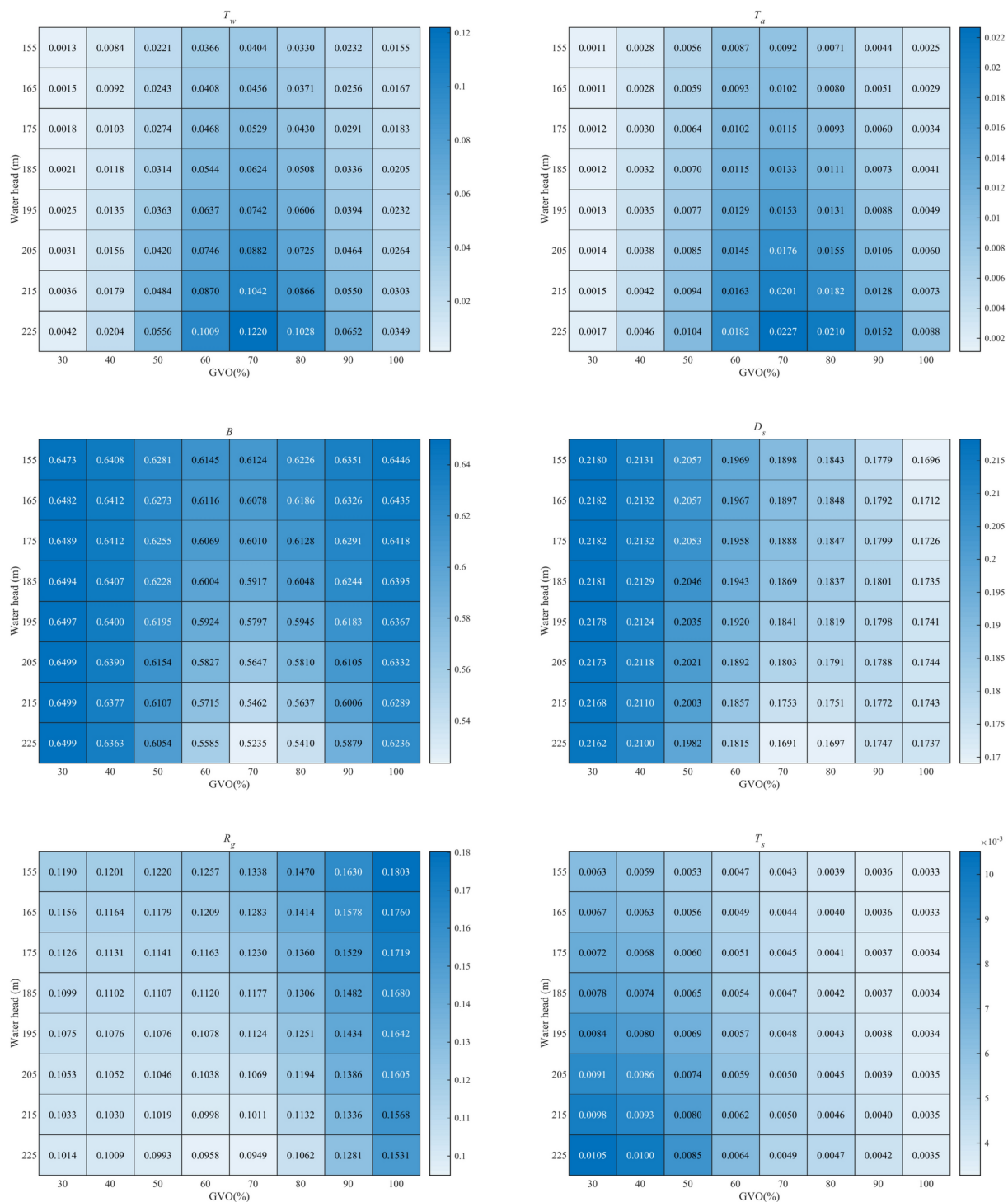


Fig. 33. S_1 under FOC.

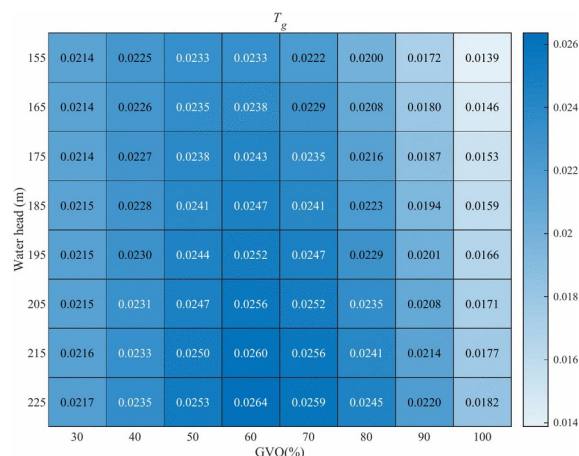


Figure 33. (continued)

Data availability

All data included in this study are available upon request by contact with the corresponding author.

Received: 25 September 2024; Accepted: 10 April 2025

Published online: 25 April 2025

References

- Walmsley, T. G. et al. Hybrid renewable energy utility systems for industrial sites: A review. *Renew. Sustain. Energy Rev.* **188**, 113802 (2023).
- Zhan, J., Wang, C., Wang, H., Zhang, F. & Li, Z. Pathways to achieve carbon emission peak and carbon neutrality by 2060: A case study in the Beijing-Tianjin-Hebei region. *China. Renew. Sustain. Energy Rev.* **189**, 113955 (2024).
- Liu, S. et al. Joint operation of mobile battery, power system, and transportation system for improving the renewable energy penetration rate. *Appl. Energy* **357**, 122455 (2024).
- Bilgili, M., Bilirgen, H., Ozbek, A., Ekinli, F. & Demirdelen, T. The role of hydropower installations for sustainable energy development in Turkey and the world. *Renew. Energy* **126**, 755–764 (2018).
- Zhao, Z. et al. A universal hydraulic-mechanical diagnostic framework based on feature extraction of abnormal on-field measurements: Application in micro pumped storage system. *Appl. Energy* **357**, 122478 (2024).
- Zhao, Z., Chen, F., Gui, Z., Liu, D. & Yang, J. Refined composite hierarchical multiscale Lempel-Ziv complexity: A quantitative diagnostic method of multi-feature fusion for rotating energy devices. *Renew. Energy* **218**, 119310 (2023).
- Liu, D., Li, C. & Malik, O. Nonlinear modeling and multi-scale damping characteristics of hydro-turbine regulation systems under complex variable hydraulic and electrical network structures. *Appl. Energy* **293**, 116949 (2021).
- Güney, M. S. & Kaygusuz, K. Hydrokinetic energy conversion systems: A technology status review. *Renew. Sustain. Energy Rev.* **14**, 2996–3004 (2010).
- Zhang, N. et al. A universal stability quantification method for grid-connected hydropower plant considering FOPI controller and complex nonlinear characteristics based on improved GWO. *Renew. Energy* **211**, 874–894 (2023).
- Fang, H., Chen, L., Dlakavu, N. & Shen, Z. Basic modeling and simulation tool for analysis of hydraulic transients in hydroelectric power plants. *IEEE Trans. Energy Convers.* **23**, 834–841 (2008).
- Chen, D., Ding, C., Ma, X., Yuan, P. & Ba, D. Nonlinear dynamical analysis of hydro-turbine governing system with a surge tank. *Appl. Math. Model.* **37**, 7611–7623. <https://doi.org/10.1016/j.apm.2013.01.047> (2013).
- Guo, W., Yang, J., Yang, W., Chen, J. & Teng, Y. Regulation quality for frequency response of turbine regulating system of isolated hydroelectric power plant with surge tank. *Int. J. Electr. Power Energy Syst.* **73**, 528–538. <https://doi.org/10.1016/j.ijepes.2015.05.043> (2015).
- Li, H., Chen, D., Zhang, H., Wang, F. & Ba, D. Nonlinear modeling and dynamic analysis of a hydro-turbine governing system in the process of sudden load increase transient. *Mech. Syst. Signal Process.* **80**, 414–428. <https://doi.org/10.1016/j.ymssp.2016.04.006> (2016).
- Liang, J., Yuan, X., Yuan, Y., Chen, Z. & Li, Y. Nonlinear dynamic analysis and robust controller design for Francis hydraulic turbine regulating system with a straight-tube surge tank. *Mech. Syst. Signal Process.* **85**, 927–946. <https://doi.org/10.1016/j.ymssp.2016.09.026> (2017).
- Wang, F., Chen, D., Xu, B. & Zhang, H. Nonlinear dynamics of a novel fractional-order Francis hydro-turbine governing system with time delay. *Chaos, Solitons Fractals* **91**, 329–338. <https://doi.org/10.1016/j.chaos.2016.06.018> (2016).
- Xue, X., Zhou, J., Xu, Y., Zhu, W. & Li, C. An adaptively fast ensemble empirical mode decomposition method and its applications to rolling element bearing fault diagnosis. *Mech. Syst. Signal Process.* **62–63**, 444–459. <https://doi.org/10.1016/j.ymssp.2015.03.002> (2015).
- Wang, L. & Guo, W. Nonlinear hydraulic coupling characteristics and energy conversion mechanism of pipeline - surge tank system of hydropower station with super long headrace tunnel. *Renew. Energy* **199**, 1345–1360. <https://doi.org/10.1016/j.renene.2022.09.061> (2022).
- Sanathanan, C. K. Accurate Low Order Model for Hydraulic Turbine-Penstock. *IEEE Trans. Energy Convers.* **2**, 196–200. <https://doi.org/10.1109/TEC.1987.4765829> (1987).
- Li, C., Zhang, N., Lai, X., Zhou, J. & Xu, Y. Design of a fractional-order PID controller for a pumped storage unit using a gravitational search algorithm based on the Cauchy and Gaussian mutation. *Inf. Sci.* **396**, 162–181. <https://doi.org/10.1016/j.ins.2017.02.026> (2017).
- Li, C. & Zhou, J. Parameters identification of hydraulic turbine governing system using improved gravitational search algorithm. *Energy Convers. Manage.* **52**, 374–381. <https://doi.org/10.1016/j.enconman.2010.07.012> (2011).

21. Vournas, C. D. Second order hydraulic turbine models for multimachine stability studies. *IEEE Trans. Energy Convers.* **5**, 239–244. <https://doi.org/10.1109/60.107216> (1990).
22. Guo, W., Yang, J., Chen, J. & Teng, Y. in *IOP Conference Series: Earth and Environmental Science*. 042004 (IOP Publishing).
23. Guo, W. & Peng, Z. Hydropower system operation stability considering the coupling effect of water potential energy in surge tank and power grid. *Renew. Energy* **134**, 846–861. <https://doi.org/10.1016/j.renene.2018.11.064> (2019).
24. Guo, W. & Yang, J. Hopf bifurcation control of hydro-turbine governing system with sloping ceiling tailrace tunnel using nonlinear state feedback. *Chaos, Solitons Fractals* **104**, 426–434. <https://doi.org/10.1016/j.chaos.2017.09.003> (2017).
25. Guo, W. & Yang, J. Dynamic performance analysis of hydro-turbine governing system considering combined effect of downstream surge tank and sloping ceiling tailrace tunnel. *Renew. Energy* **129**, 638–651. <https://doi.org/10.1016/j.renene.2018.06.040> (2018).
26. Guo, W. & Yang, J. Stability performance for primary frequency regulation of hydro-turbine governing system with surge tank. *Appl. Math. Model.* **54**, 446–466. <https://doi.org/10.1016/j.apm.2017.09.056> (2018).
27. Guo, W., Yang, J., Chen, J. & Wang, M. Nonlinear modeling and dynamic control of hydro-turbine governing system with upstream surge tank and sloping ceiling tailrace tunnel. *Nonlinear Dyn.* **84**, 1383–1397. <https://doi.org/10.1007/s11071-015-2577-0> (2016).
28. Guo, W., Yang, J., Wang, M. & Lai, X. Nonlinear modeling and stability analysis of hydro-turbine governing system with sloping ceiling tailrace tunnel under load disturbance. *Energy Convers. Manage.* **106**, 127–138. <https://doi.org/10.1016/j.enconman.2015.09.026> (2015).
29. Xu, X. & Guo, W. Stability of speed regulating system of hydropower station with surge tank considering nonlinear turbine characteristics. *Renew. Energy* **162**, 960–972. <https://doi.org/10.1016/j.renene.2020.08.098> (2020).
30. Daijian, L., Yang, T. & Zuyi, S. Hopf bifurcation analysis of hydraulic turbine governing systems with elastic water hammer effect. *Journal of Vibration Engineering* **20** (2007).
31. Zeng, W., Yang, J. & Yang, W. Instability analysis of pumped-storage stations under no-load conditions using a parameter-varying model. *Renew. Energy* **90**, 420–429. <https://doi.org/10.1016/j.renene.2016.01.024> (2016).
32. Lai, X., Huang, H., Zheng, B., Li, D. & Zong, Y. Nonlinear modeling and stability analysis of asymmetric hydro-turbine governing system. *Appl. Math. Model.* **120**, 281–300. <https://doi.org/10.1016/j.apm.2023.03.012> (2023).
33. Guo, W. & Zhu, D. Nonlinear modeling and operation stability of variable speed pumped storage power station. *Energy Sci. Eng.* **9**, 1703–1718. <https://doi.org/10.1002/ese3.943> (2021).
34. Zhao, Z., Yang, J., Yang, W., Hu, J. & Chen, M. A coordinated optimization framework for flexible operation of pumped storage hydropower system: Nonlinear modeling, strategy optimization and decision making. *Energy Convers. Manage.* **194**, 75–93. <https://doi.org/10.1016/j.enconman.2019.04.068> (2019).
35. Changyu, L. et al. Refined Modeling of Hydraulic Prime Mover and Its Governing System for Hydropower Generation Unit. *Power System Technology* **39** (2015).
36. Faris, H., Aljarah, I., Al-Betar, M. A. & Mirjalili, S. Grey wolf optimizer: A review of recent variants and applications. *Neural Comput. Appl.* **30**, 413–435 (2018).
37. Li, C., Mao, Y., Zhou, J., Zhang, N. & An, X. Design of a fuzzy-PID controller for a nonlinear hydraulic turbine governing system by using a novel gravitational search algorithm based on Cauchy mutation and mass weighting. *Appl. Soft Comput.* **52**, 290–305. <https://doi.org/10.1016/j.asoc.2016.10.035> (2017).
38. Zhang, N., Li, C., Li, R., Lai, X. & Zhang, Y. A mixed-strategy based gravitational search algorithm for parameter identification of hydraulic turbine governing system. *Knowl.-Based Syst.* **109**, 218–237. <https://doi.org/10.1016/j.knsys.2016.07.005> (2016).
39. Liu, D. et al. Stability analysis of hydropower units under full operating conditions considering turbine nonlinearity. *Renew. Energy* **154**, 723–742. <https://doi.org/10.1016/j.renene.2020.03.038> (2020).
40. Lai, X., Li, C., Guo, W., Xu, Y. & Li, Y. Stability and dynamic characteristics of the nonlinear coupling system of hydropower station and power grid. *Commun. Nonlinear Sci. Numer. Simul.* **79**, 104919. <https://doi.org/10.1016/j.cnsns.2019.104919> (2019).
41. Xu, B., Chen, D., Patelli, E., Shen, H. & Park, J.-H. Mathematical model and parametric uncertainty analysis of a hydraulic generating system. *Renew. Energy* **136**, 1217–1230 (2019).
42. ZY, S. *Analysis of hydro-turbine governing system*. (Beijing: China Water & Power Press, UK, 1991).
43. Zhang, H., Chen, D., Xu, B. & Wang, F. Nonlinear modeling and dynamic analysis of hydro-turbine governing system in the process of load rejection transient. *Energy Convers. Manage.* **90**, 128–137 (2015).
44. C, W., DH, Z. & ZX, T. Hopf bifurcation analysis of nonlinear hydro turbine governing system. *Water Resour Power* **36**, 148–151 (2018).
45. Saltelli, A. et al. Variance based sensitivity analysis of model output. Design and estimator for the total sensitivity index. *Comput. Phys. Commun.* **181**, 259–270 (2010).

Acknowledgements

The Project was Supported by the open fund for Jiangsu Key Laboratory of Advanced Manufacturing Technology (Grant No. HGAMTL-2203), the Major Basic Research Project of the Natural Science Foundation of the Jiangsu Higher Education Institutions (Grant No. 21KJA460010), the Natural Science Foundation of the Jiangsu Higher Education Institutions of China (No. 24KJD480002, No. 24KJD480001), Natural Science Foundation of Nantong Municipality (No. JCZ2023016) and Natural Science Foundation of Hubei Province (Grant No. 2022CFB935).

Author contributions

Chen Feng: Investigation, Methodology, Simulation, Writing – original draft. Na Sun: Investigation, Methodology, Simulation, Writing – original draft. Chuang Zheng: Conceptualization, Data curation, Investigation, Writing-original draft. Yongqi Zhu: Data curation, Validation. Nan Zhang: Supervision, Funding acquisition, Writing-review & editing. Yahui Shan: Supervision, Formal analysis, Funding acquisition, Visualization. Liping Shi: Visualization, Writing-review & editing. Xiaoming Xue: Funding acquisition, Visualization, Writing-review & editing.

Funding

Open fund for Jiangsu Key Laboratory of Advanced Manufacturing Technology, HGAMTL2203, HGAMTL2203, HGAMTL2203, HGAMTL2203, Natural Science Foundation of the Jiangsu Higher Education Institutions of China, 24KJD480001, 24KJD480002, 24KJD480002, 24KJD480002, 24KJD480002, Natural Science Foundation of Hubei Province, 2022CFB935, Major Basic Research Project of the Natural Science Foundation of the Jiangsu Higher Education Institutions, 21KJA460010, Natural Science Foundation of Nantong Municipality, JCZ2023016.

Declaration

Competing interests

The authors declare no competing interests.

Additional information

Correspondence and requests for materials should be addressed to N.Z. or Y.S.

Reprints and permissions information is available at www.nature.com/reprints.

Publisher's note Springer Nature remains neutral with regard to jurisdictional claims in published maps and institutional affiliations.

Open Access This article is licensed under a Creative Commons Attribution-NonCommercial-NoDerivatives 4.0 International License, which permits any non-commercial use, sharing, distribution and reproduction in any medium or format, as long as you give appropriate credit to the original author(s) and the source, provide a link to the Creative Commons licence, and indicate if you modified the licensed material. You do not have permission under this licence to share adapted material derived from this article or parts of it. The images or other third party material in this article are included in the article's Creative Commons licence, unless indicated otherwise in a credit line to the material. If material is not included in the article's Creative Commons licence and your intended use is not permitted by statutory regulation or exceeds the permitted use, you will need to obtain permission directly from the copyright holder. To view a copy of this licence, visit <http://creativecommons.org/licenses/by-nc-nd/4.0/>.

© The Author(s) 2025